



**HAL**  
open science

## Differential interferometry of the rapid rotator Regulus

M. Hadjara, R. Petrov, S. Jankov, P. Cruzalèbes, A. Spang, S. Lagarde

► **To cite this version:**

M. Hadjara, R. Petrov, S. Jankov, P. Cruzalèbes, A. Spang, et al.. Differential interferometry of the rapid rotator Regulus. Monthly Notices of the Royal Astronomical Society, 2018, 480 (1), pp.1263-1277. 10.1093/mnras/sty1893 . hal-02323504

**HAL Id: hal-02323504**

**<https://hal.science/hal-02323504>**

Submitted on 14 Jan 2022

**HAL** is a multi-disciplinary open access archive for the deposit and dissemination of scientific research documents, whether they are published or not. The documents may come from teaching and research institutions in France or abroad, or from public or private research centers.

L'archive ouverte pluridisciplinaire **HAL**, est destinée au dépôt et à la diffusion de documents scientifiques de niveau recherche, publiés ou non, émanant des établissements d'enseignement et de recherche français ou étrangers, des laboratoires publics ou privés.



Distributed under a Creative Commons Attribution 4.0 International License

# Differential interferometry of the rapid rotator Regulus

M. Hadjara,<sup>1,2,3\*</sup> R. G. Petrov,<sup>2</sup> S. Jankov,<sup>4</sup> P. Cruzalèbes,<sup>2</sup> A. Spang<sup>2</sup> and S. Lagarde<sup>2</sup>

<sup>1</sup>*Instituto de Astronomía, Universidad Católica del Norte, Av. Angamos, 0610 Antofagasta, Chile*

<sup>2</sup>*Université de Nice–Sophia Antipolis (UNS), Centre National de la Recherche Scientifique (CNRS), Observatoire de la Côte d’Azur (OCA), Laboratoire J. L. Lagrange, UMR 7293, Campus Valrose, 06108 Nice Cedex 2, France*

<sup>3</sup>*Centre de Recherche en Astronomie, Astrophysique et Géophysique (CRAAG), Route de l’Observatoire, B. P. 63, Bouzareah, 16340 Alger, Algeria*

<sup>4</sup>*Astronomical Observatory, Volgina 7, PO Box 74, 11060 Belgrade, Serbia*

Accepted 2018 July 12. Received 2018 July 1; in original form 2017 October 9

## ABSTRACT

We analyse interferometric data obtained for Regulus with AMBER (Astronomical Multi-BEam combineR) at high spectral resolution ( $\lambda/\delta\lambda \approx 12\,000$ ) across the Br $\gamma$  spectral line. The study of the photocentre displacement allows us to constrain a large number of stellar parameters – equatorial radius  $R_{\text{eq}}$ , equatorial velocity  $V_{\text{eq}}$ , inclination  $i$ , rotation-axis position angle  $PA_{\text{rot}}$  and flattening – with an estimation of gravity-darkening coefficient  $\beta$  using previously published theoretical results. We use the Simulation Code of Interferometric-observations for ROtators and CirCumstellar Objects (SCIROCCO), a semi-analytical algorithm dedicated to fast rotators. We chose Regulus because it is a very well-known edge-on star, for which an alternative approach is needed to check the previously published results. Our analysis showed that a significant degeneracy of solution is present. By confronting the results obtained by differential interferometry with those obtained by conventional long-base interferometry, we obtain similar results (within the uncertainties), thereby validating our approach, where  $V_{\text{eq}}$  and  $i$  are found separately. From the photocentre displacement, we can independently deduce  $PA_{\text{rot}}$ . We use two minimization methods to restrict observed stellar parameters via a fast rotator model: a non-stochastic method ( $\chi^2$  fit) and a stochastic one (Markov Chain Monte Carlo method), in order to check whether the correct global minimum is achieved, particularly with respect to the degeneracies of the gravity-darkening parameter  $\beta$ , where we demonstrate, using a quantitative analysis of parameters, that estimation of  $\beta$  is easier for stars with an inclination angle of around  $45^\circ$ .

**Key words:** methods: numerical – methods: observational – techniques: high angular resolution – techniques: interferometric – stars: individual: Regulus.

## 1 INTRODUCTION

### 1.1 Optical interferometry of rapid rotators

Stellar rotation was measured for the first time by interferometry, from the photocentre displacements by Lagarde (1994), on the slow rotator Aldebaran, which was observed in 1988 at OHP (Observatoire de Haute-Provence) through the 152-cm telescope by the speckle differential interferometry method. Results obtained by interferometry on fast rotators were summarized by Jankov (2011) and van Belle (2012). The extreme stellar flattening induced by rotation was measured using interferometry by Domiciano de Souza et al. (2003) on Achernar ( $R_{\text{eq}}/R_{\text{pol}} = 1.56 \pm 0.05$ ), using VLTI/VINCI

(Very Large Telescope Interferometer/VLT Interferometer Commissioning Instrument) with a dense  $(u, v)$  coverage. The first image reconstruction of the surface of a fast rotator, showing the gravity-darkening effect (von Zeipel 1924a,b), was on Altair (Monnier et al. 2007) from CHARA (Center for High Angular Resolution Astronomy) observations, inferring several fundamental parameters: inclination, position angle, effective temperature and polar and equatorial radii.

Inspired by the early works of Labeyrie (1975), Beckers (1982) proposed the differential speckle interferometry technique, using the chromatic displacement of the speckle photocentre given by the first-order term of the phase of the spatial Fourier transform of the sky brightness according to the MacLaurin series (Jankov et al. 2001). This technique has been extended to a wider range of wavelengths and applied to long-baseline interferometry by Petrov (1988, 1989), who established the fundamentals of the differential interferometry (DI) technique. This allowed researchers, for the first time, to measure simultaneously the angular separation and

\* E-mail: massinissa.hadjara@gmail.com (MH); romain.petrov@oca.eu (RGP); sjankov@aob.rs (SJ)

the radial velocity difference of the two stellar components of the binary Capella (Petrov & Lagarde 1992), using the photocentre as a function of the wavelength.

The combination of high spatial and high spectral resolution allows us to measure physical properties of fast rotators beyond the diffraction limit, as shown by Domiciano de Souza et al. (2012) and Hadjara et al. (2014), who used the differential phases from AMBER/VLTI (Astronomical Multi-BEam combineR). Indeed, AMBER (Petrov et al. 2007) is a spectro-interferometric instrument designed specifically to go well beyond the resolution limit (e.g. Meilland et al. 2007; Le Bouquin et al. 2009).

Optical interferometry provides several types of measures, such as the absolute visibility, differential visibility and closure phase (Petrov et al. 2007), but in this article we focus only on differential phase and vectorial photocentre displacement.

## 1.2 The fast rotator Regulus

$\alpha$  Leo A (HR 3982, HD 87901), one of the brightest stars of the sky, is a binary system, the brighter primary component of which is referred to as Regulus throughout this article. Regulus is an edge-on and flattened nearby star, which is in rapid rotation. In the following, we summarize the spectrophotometric and interferometric information of our target separately.

### 1.2.1 Information from spectroscopy and photometry

With magnitude  $V = 1.40$  (van Belle & von Braun 2009), Regulus has been identified as a fast rotator by Slettebak (1954), who determined by spectroscopy its high rotational velocity  $V_{\text{eq}} \sin i = 352 \pm 7.5 \text{ km s}^{-1}$ , i.e. 96 per cent of its critical velocity.

$\alpha$  Leo is a multiple stellar system composed of at least two binaries. The A component of the system ( $\alpha$  Leo A, HD 87901) has recently been discovered to be a spectroscopic binary. The brighter companion (Regulus) was classified as a main-sequence B7V star by Johnson & Morgan (1953) and more recently as a subgiant B8IV star by Gray et al. (2003), with mass  $\sim 4 M_{\odot}$  (Che et al. 2011, and references therein). Gies et al. (2008) argue that the fainter companion of  $\alpha$  Leo A is probably a white dwarf or a M4 V star of mass  $\sim 0.3 M_{\odot}$  and an orbital period of 40.11 days and that the magnitude difference of the fainter component with respect to Regulus in the  $K$  band is close to  $\Delta m_K \approx 10$  ( $\sim 10^{-4}$  of the flux ratio) and 6 ( $\sim 4 \times 10^{-3}$  of the flux ratio), for the cases of a white dwarf and an M4 V star companion, respectively. Thus, the flux of the companion has no influence on our analysis (Bry and adjacent continuum), nor on the interferometry presented by McAlister et al. (2005) and Che et al. (2011). For this reason, only extraordinary activity of the fainter star, reflected as a several orders of magnitude enhancement of the  $\text{Br}_{\gamma}$  emission, could eventually affect our results.  $\alpha$  Leo A has a companion, which is in fact a system of two other components (B and C), which together form a binary system (McAlister et al. 2005). The B component ( $\alpha$  Leo B; HD 87884) is an  $\sim 0.8 M_{\odot}$  star of spectral type K2V, while the C component is a very faint M4V star with a mass of  $\sim 0.2 M_{\odot}$ . The Washington Double Star Catalog (Mason et al. 2001) lists a D component, also having a common proper motion with the system and a separation of  $\approx 3.6$  arcmin from the A component, while the B–C subsystem is located  $\approx 3$  arcmin from the A component.

Iorio (2008) studied the possible correction of the Keplerian period due to the quadrupole mass moment induced by the oblateness

of Regulus. Although this correction could be measured in principle, the total uncertainty in the Keplerian period (0.02 days from Gies et al. 2008) due to errors in the system parameters (mostly in the velocity semi-amplitude and the mass of Regulus) is larger than the correction by about two orders of magnitude. Its distance is  $d = 24.3 \pm 0.2$  pc, according to van Leeuwen (2007), and  $d = 23.759 \pm 0.045$  pc, according to van Belle & von Braun (2009). Its mass is  $M = 4.15 \pm 0.06 M_{\odot}$  from the  $Y^2$  stellar evolution model (Yi et al. 2001; Yi, Kim & Demarque 2003; Demarque et al. 2004),  $3.66^{+0.79}_{-0.28} M_{\odot}$  from Che et al. (2011) according to the oblateness mass method of Zhao et al. (2009) and  $3.80 \pm 0.6 M_{\odot}$  from Malagnini & Morossi (1990) according to the evolutionary tracks of Maeder & Meynet (1989). Its age is estimated at between 150 Myr (Gerbaldi, Faraggiana & Balin 2001) and 1 Gyr (Rappaport, Podsiadlowski & Horev 2009). Its effective temperature  $T_{\text{eff}}$  is  $12\,460 \pm 200$  K according to Malagnini & Morossi (1990) and  $11\,960 \pm 80$  K according to Gray et al. (2003). Its metallicity  $[M/H]$  is 0.0 according to Gray et al. (2003).

### 1.2.2 Interferometric observations of Regulus

The first interferometric observations of this star were made with the Narrabri Intensity Interferometer by Hanbury Brown, Davis & Allen (1974). Because of the poor ( $u, v$ )-plane coverage, only information about its size could be obtained, with an equatorial angular diameter  $\mathcal{D}_{\text{eq}} = 1.32 \pm 0.06$  mas. Using CHARA array observations in the  $K$  band, McAlister et al. (2005) measured for the first time the inclination of its rotation axis  $i = 90^{\circ}_{-15}$  and characterized other physical parameters, such as the rotation-axis position angle  $PA_{\text{rot}} = 265.5 \pm 2.8^{\circ}$ , rotational equatorial velocity  $V_{\text{eq}} = 317^{+3}_{-85} \text{ km s}^{-1}$ , fractional rotational velocity  $V_{\text{eq}}/V_{\text{crit}} = 0.86 \pm 0.03$ , equatorial and polar radii  $R_{\text{eq}} = 4.16 \pm 0.08 R_{\odot}$  and  $R_{\text{pol}} = 3.15 \pm 0.06 R_{\odot}$ , equatorial and polar effective temperatures  $T_{\text{eq}} = 10\,314 \pm 1000$  K and  $T_{\text{pol}} = 15\,400 \pm 1400$  K, mass  $M$ , luminosity  $L$ , gravity-darkening coefficient  $\beta$  (defined as  $T_{\text{eff}} \propto g_{\text{eff}}^{\beta}$  by von Zeipel 1924a, where  $T_{\text{eff}}$  and  $g_{\text{eff}}$  are local effective temperature and gravity, respectively), distance  $d$  and interstellar extinction  $A_v$ . More recently, Che et al. (2011) used the CHARA/MIRC (Michigan Infra-Red Combiner) instrument to produce maps of  $\alpha$  Leo in the  $H$  band and deduced inclination angle  $i = 86.3^{\circ}_{-1.6^{\circ}}^{+1.0^{\circ}}$  and gravity-darkening coefficient  $\beta = 0.188^{+0.012}_{-0.029}$ , which is consistent (within the uncertainties) with the results of McAlister et al. (2005). Thus, interferometry revealed that Regulus is an edge-on star with an inclination angle of  $i \sim 90^{\circ}$ , rotationally flattened with an oblateness ratio (equatorial-to-polar radii minus 1;  $R_{\text{eq}}/R_{\text{pol}} - 1$ ) reported between  $0.325 \pm 0.036$  (angular diameter  $\mathcal{D}_{\text{eq}} = 1.65 \pm 0.02$  mas) and  $0.307 \pm 0.030$  ( $\mathcal{D}_{\text{eq}} = 1.61^{0.03}_{-0.02}$  mas; McAlister et al. 2005; Che et al. 2011).

Table 1 summarizes the fundamental parameters of Regulus.

## 1.3 Structure of the article

In this article, we describe differential interferometry with high spectral resolution observations ( $R \simeq 12\,000$ ) in the  $K$  band of the rapid rotator Regulus; we focus on the parameters that can be extracted from the photocentre displacement, eventually in combination with the broadened spectral line profile. We compare this in detail with the parameters obtained from broad-band interferometric images and discuss those values that are inferred or improved by the comparison and then the combination of both techniques.

**Table 1.** Fundamental stellar parameters of  $\alpha$  Leo found in the literature.

Parameter	Value
Angular diameter ( $\mathcal{D}_{\text{eq}}$ )	$1.65 \pm 0.02$ mas (1) $1.61_{-0.02}^{+0.03}$ mas (2)
Oblateness ratio ( $R_{\text{eq}}/R_{\text{pol}} - 1$ )	$0.325 \pm 0.036$ (1) $0.307 \pm 0.030$ (2)
Distance ( $d$ )	$24.3 \pm 0.2$ pc (3) $23.759 \pm 0.045$ pc (4) $4.15 \pm 0.06 M_{\odot}$ (5)
Mass ( $M$ )	$3.66_{-0.28}^{+0.79} M_{\odot}$ (2) $3.80 \pm 0.6 M_{\odot}$ (6)
Age	50–200 Myr (7) $\geq 1$ Gyr (8)
Eff. temperature ( $T_{\text{eff}}$ )	$12460 \pm 200$ K (6) $11960 \pm 80$ K (9)
Metallicity ( $[M/H]$ )	0.0 (9)
Rotation-axis position angle $PA_{\text{rot}}$	$265.5 \pm 2.8^{\circ}$ (10) $258_{-1}^{+2}$ (11)
Rotation-axis inclination angle $i$	$90_{-15}^{+0}$ (10) $85.3_{-1.6}^{+1}$ (11)

Notes:

- (1) McAlister et al. (2005); (2) Che et al. (2011);  
 (3) van Leeuwen (2007); (4) van Belle & von Braun (2009);  
 (5) Demarque et al. (2004); (6) Malagnini & Morossi (1990);  
 (7) Gerbaldi et al. (2001); (8) Rappaport et al. (2009);  
 (9) Gray et al. (2003); (10) McAlister et al. (2005);  
 (11) Che et al. (2011).

The present article is organized as follows. In Section 2, we present the observations and data reduction for Regulus. In Section 3, we study the photocentre displacement of our target, where we deduce  $PA_{\text{rot}}$  directly from the observed photocentre displacements. In Section 4, we present the model that was used in order to interpret our measurements and discuss the constraints that they place on the gravity-darkening parameter  $\beta$  of Regulus. In Section 5, we fit the fundamental parameters of Regulus, using a non-stochastic method ( $\chi^2$ ) and a stochastic one (Markov Chain Monte Carlo (MCMC) method). In Section 6, we summarize the computed accuracy limits that we can achieve with the quality of our data and the probability spaces of the couple ( $\beta$ ,  $i$ ) of Regulus. In Section 7, we analyse the results and open the discussion to a broader study of fast-rotating stars observed with VLTI-AMBER by DI.

## 2 OBSERVATIONS AND DATA REDUCTION

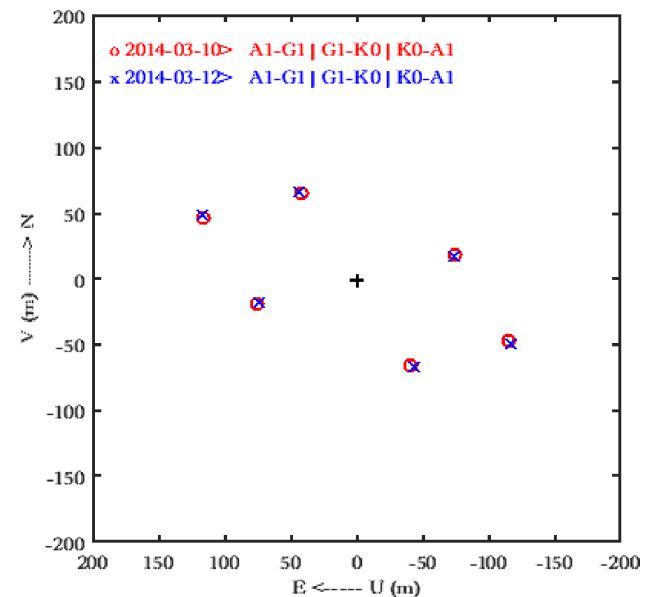
Regulus was observed with the AMBER/VLTI instrument located at Cerro Paranal, Chile, with the Auxiliary Telescopes. The fringes were stabilized using FINITO (Fringe-tracking Instrument of Nice and Torino) (Mérand et al. 2012) as a fringe tracker, allowing us to use a detector integration time (DIT) of 3 s for 20 exposures. The observations have been performed using the high spectral resolution mode of AMBER ( $\lambda/\delta\lambda \approx 12000$ ). Table 2 provides the observation log of Regulus.

The differential phase  $\phi_{\text{diff}}$  obtained from the data reduction algorithm is related to the object's Fourier phase  $\phi_{\text{obj}}$  by (e.g. Millour et al. 2006, 2011)

$$\phi_{\text{diff}}(u, v) = \phi_{\text{obj}}(u, v) - a(u, v) - b(u, v)/\lambda, \quad (1)$$

**Table 2.** VLTI/AMBER observations of Regulus and its calibration stars using AT triplet A1-G1-K0. Note that the detector integration time (DIT)=3 s, frame number per exposure NDIT=20 and number of all used exposures NEXP=32 for the first night (2014 March 10) and 22 for the second night (2014 March 12).

Object	Date & time	Baseline length	Baseline PA
		$B_{\text{proj}}(\text{m})$	$PA(^{\circ})$
60 Cnc	2014-03-10 T03:09	75,81,128	103,34,67
Regulus	2014-03-10 T03:48	78,77,125	104,32,68
w Cen	2014-03-10 T04:30	73,87,129	88,14,47
w Cen	2014-03-10 T04:44	74,87,129	90,16,50
$\epsilon$ Cma	2014-03-12 T02:15	75,87,116	124,36,76
Regulus	2014-03-12 T03:59	76,79,127	104,33,68
w Cen	2014-03-12 T04:45	75,87,129	92,17,51
$\iota$ Cen	2014-03-12 T07:17	80,88,126	113,30,69


**Figure 1.**  $(u, v)$  coverage for our VLTI/AMBER observations of Regulus.

where the spatial frequency coordinates  $u$  and  $v$  depend on the wavelength  $\lambda$ , the projected baseline length  $B_{\text{proj}}$  and the baseline position angle  $PA$  (from north to east;  $u = B_{\text{proj}} \sin(PA)/\lambda$  and  $v = B_{\text{proj}} \cos(PA)/\lambda$ ). The parameters  $a$  and  $b$  correspond to an offset and a slope, given in appropriate units.

The corresponding  $(u, v)$  coverage is shown in Fig. 1, where the  $(u, v)$  plane is spanned over  $\sim 1.5$  h night $^{-1}$ . Note the rather poor sampling of the Fourier space. According to Table 2, the  $(u, v)$  points for the date 2014 March 10 are represented by red circles and those for the date 2014 March 12 by blue crosses.

Data have been reduced using version 3.0.9 of the AMDLIB software (Chelli, Utrera & Duvert 2009; Tatulli et al. 2007). We adopt a mild frame selection based on fringe signal-to-noise (S/N) and geometric flux-to-noise thresholds greater than unity. Our dataset includes the stellar spectrum, differential visibilities, differential phases and closure phases.

### 2.1 Spectrum

The high spectral resolution mode of AMBER leads to a velocity resolution of  $\approx 25$  km s $^{-1}$ . The projected equatorial rotational velocities  $V_{\text{eq}} \sin i$  above  $\sim 150$  km s $^{-1}$  of Regulus ensure that the Br $\gamma$  line

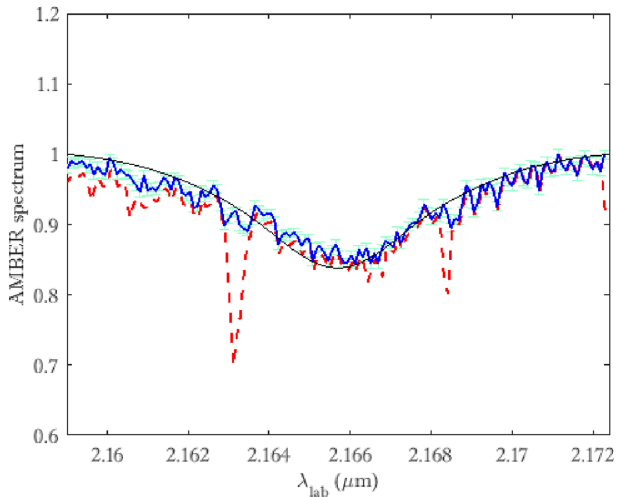


**Figure 2.** AMBER spectrum of Regulus in the Br $\gamma$  line. The dashed thick red curve is the raw spectrum showing two telluric lines. The full thick blue curve is the Regulus spectrum, with its error bars in green. The thin dark line represents our best model, which is discussed in Section 5.1.

is sampled by six spectral channels. Thus rotation effects should be taken into account when modelling phase signatures.

Fig. 2 shows the normalized observed flux of Regulus as observed (dashed red curve) and after correction (blue line). The smooth black curves superimposed on the observations show our best model, which is discussed in Section 5.1. The normalized observed flux was corrected by removing both strong tellurics and performing a wavelength calibration. We converted the wavelength scale to the laboratory frame using the Regulus heliocentric velocity of  $5.90 \pm 2.40 \text{ km s}^{-1}$  measured by Anderson & Francis (2012) and the IRAF package,<sup>1</sup> in order to convert the observed velocity to the heliocentric frame ( $RV = -10.195 \text{ km s}^{-1}$ , the average of both nights:  $-9.69 \text{ km s}^{-1}$  for 2014 March 10 and  $-10.70 \text{ km s}^{-1}$  for 2014 March 12).

## 2.2 Visibilities

Fig. 3 shows the observed visibilities, superimposed on our best model (black line), which is discussed in Section 5.1. The second baselines ( $B_{\text{proj}} \approx 78 \text{ m}$  and  $PA \approx 32^\circ$ ), which are the closest to the polar direction of Regulus, are those with visibility closest to 1.

The baseline values show that the angular resolution  $\lambda/B$  is always larger than 3.5 mas. As the largest diameter of Regulus is smaller than 1.7 mas, the source is not resolved enough for image reconstruction, as confirmed by our closure phases, which are equal to zero within the noise, shown in Fig. 4 below.

The longest projected baseline in the polar direction is  $\sim 74 \text{ m}$ . With our 0.04 error in the visibility, an angular diameter of 1.1 mas is measured with typically 0.7 mas accuracy, which means that it can be any value smaller than 1.8 mas (or even 2.5 mas at  $2\sigma$  level). In the equatorial direction, the longest projected baseline is  $\sim 125 \text{ m}$  and a 1.6-mas diameter is measured with an accuracy of typically 0.16 mas. We see that the absolute visibilities of our VLTI baselines in the K band can be used to estimate the largest diameter of Regulus

with an accuracy comparable to previously published results, but this is useless to constrain the oblateness with any useful accuracy. In other words, our absolute visibility measurements cannot resolve the oblateness of Regulus, nor its position angle, and cannot give any access to the consequences of its rapid rotation. This is confirmed by our measurements with  $V=1$  within the noise on at least one baseline in each observation.

Regulus is marginally resolved and its visibilities are constant and flat (the average visibility of the six  $(u, v)$  points is around 0.9) within the noise. The visibilities are flat because we are at high spectral resolution ( $R \sim 12000$ ); the variation of the wavelength range is so weak that the slopes of the visibilities are indistinguishable within the noise. Qualitatively, our wavelength range is between 2.15 and 2.17  $\mu\text{m}$ . The radius of Regulus is  $\approx 1.63 \text{ mas}$  and our largest baseline is 125 m. With a simple uniform disc model, we obtain a visibility of 0.830 for  $\lambda = 2.15 \mu\text{m}$  and 0.833 for  $\lambda = 2.17 \mu\text{m}$  (a difference of 0.3 per cent in terms of visibility between the first and the last wavelength).

## 2.3 Differential phase, vectorial photocentre displacement and closure phase

The differential phase is the variation of the phase through a spectral line with respect to the phase in the continuum forced to zero (see equation 1). In resolved sources, the differential phase boosts the imaging capability (Millour et al. 2011). In non-resolved sources, the differential phase is proportional to the photocentre variation of the source with wavelength  $\epsilon(\lambda)$ , with respect to the photocentre of the source in the continuum  $\epsilon(\lambda_c)$ , as follows:

$$\phi_{ij}(\lambda) = 2\pi\epsilon(\lambda)\mathbf{B}_{ij}/\lambda. \quad (2)$$

As soon as it is measured on two baselines  $\mathbf{B}_{ij}$  ( $i \neq j$ ), it yields the vectorial photocentre displacement  $\epsilon(\lambda) - \epsilon(\lambda_c)$ . As the absolute photocentre of the source is unknown, we decide by convention that the photocentre of the source in the continuum (or in the reference channel) is the origin of the coordinate system and that  $\epsilon(\lambda_c) = 0$ . To simplify the equations, in the following we shall just use  $\epsilon(\lambda)$ , but we have to remember that it is defined in a coordinate system with the photocentre in the spectral reference channel at its origin. In non-resolved sources, the differential phase decreases like  $\mathcal{D}_{\text{eq}}/(\lambda/B)$ . As for spectroastrometry on single apertures (Whelan et al. 2015), it yields a photocentre variation vector at the source much smaller than the diffraction limit. This makes the differential phase the optical interferometry measure with the highest ‘super-resolution’ potential. For example, with a differential phase accuracy of the order of 5 milliradians (mrad), we have a photocentre displacement accuracy of 4 microarcsec ( $\mu\text{as}$ ) with AMBER on the VLTI (achieved by Le Bouquin et al. 2009, on Fomalhaut). The vectorial photocentre displacement yields the position angle of the rotation axis (e.g. Fomalhaut by Le Bouquin et al. 2009), angular sizes and rotation velocities. It allows us to separate the different components of the source with different spectral characteristics or radial velocities spatially and spectrally. This has been achieved first for non-resolved slow rotators by Lagarde (1994) and for fast rotators by Domiciano de Souza et al. (2003).

The visibilities are also quasi-flat for the Br $\gamma$  line and, obviously, all closure phases are equal to zero. In this case and according to Petrov (1989) (and after that Lachaume (2003), using the moment of the flux distribution, which is  $\approx$  object size/spatial resolution), who have demonstrated that the phase ( $\phi$ ) is proportional to the first order of this quantity, the visibility modulus ( $1 - |V|^2$ ) is proportional to the second order and the closure phase ( $\Psi$ ) to the third.

<sup>1</sup>IRAF is distributed by the National Optical Astronomy Observatories, which are operated by the Association of Universities for Research in Astronomy, Inc., under cooperative agreement with the National Science Foundation.

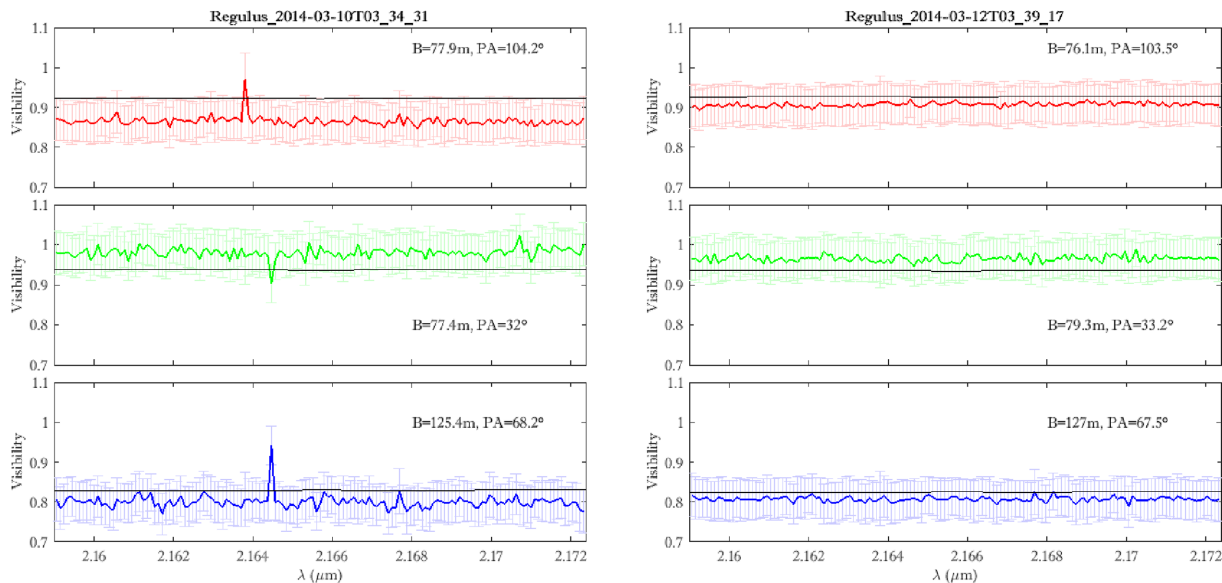


**Figure 3.** The six observed visibilities of Regulus as coloured thick lines, with uncertainties overlotted from the modelling visibilities as black thin lines. The equatorial radius of our best model corresponds to  $R_{\text{eq}} = 4.16 \pm 0.24 R_{\odot}$ , the polar radius is  $R_{\text{pol}} = 3.08 \pm 0.27 R_{\odot}$  and  $PA_{\text{rot}} = 251 \pm 2^{\circ}$  (see Section 5.1).

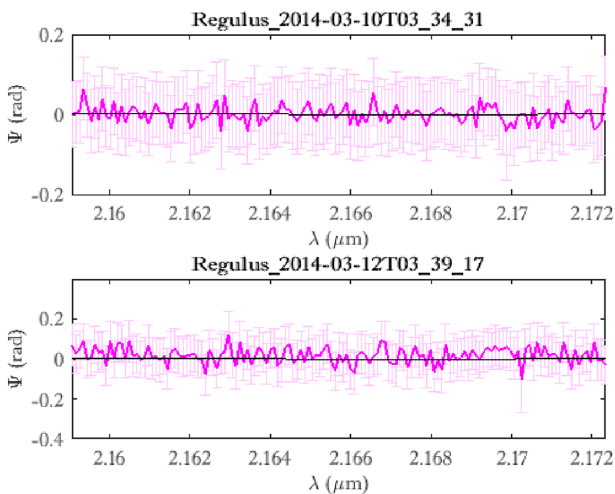


**Figure 4.** Both observed closure phases of Regulus as coloured thick lines, with uncertainties overlotted from the modelling as black thin lines and with the same parameters as Fig.3 (see Section 5.1).

Thus, only the differential phase can give useful angular resolution information. All the baselines can therefore be projected on to two photocentre coordinates, as soon as we have baselines in at least two different directions. This means that we obtain  $\epsilon_{\alpha}$  in the right ascension (east to west) direction and  $\epsilon_{\delta}$  in the declination (south to north) direction, from an average of the projections of all baselines on to these two directions. The contribution of each baseline is weighted by its signal-to-noise ratio (SNR).

We are therefore in the situation in which all differential phases given by equation (2) can be projected on to two orthogonal axes or plotted as a vector (Fig. 5).

### 3 INDEPENDENT DETERMINATION OF $PA_{\text{ROT}}$

In this section, we deduce independently the  $PA_{\text{rot}}$  of the star, directly and only from observed photocentre displacements, as has been done in the past: first by Petrov & Lagarde (1992) on the binary Cappella, by Lagarde (1994) on the slow rotator Aldebaran, then by Le Bouquin et al. (2009) on Fomalhaut and its circumstellar debris disc.  $PA_{\text{rot}}$  is defined as the angle from north to east until the stellar rotation axis at the visible stellar pole is reached. With this definition and by a simple linear fit of our data ( $\epsilon_{\alpha} = a_1 \epsilon_{\delta} + a_2$ ), we find  $PA_{\text{rot}}$  as the slope of the line:  $PA_{\text{rot}} = \pi + \arctan(a_1) = 250.73^{\circ} \pm 3^{\circ}$  ( $+\pi$  because of the first visible stellar pole, which is to the west of the SED). This value is close to the previous results of  $PA_{\text{rot}}$  (McAlister et al. 2005; Che et al. 2011). Fig. 5 shows the photocentre displacement of Regulus, which is in the same equatorial direction of our target.

The vectorial representation in Fig. 5 gives the position angle of the rotation vector directly. Differential interferometry allows us to find the exact orientation of the rotation vector. A comparison with the motion of sources close to Regulus (its companions in the first place) could give constraints on the history of Regulus, but this is outside the scope of this article.

Once  $PA_{\text{rot}}$  is known, using elementary coordinate frame rotation rules we can deduce the equatorial and polar photocentre displacements ( $\epsilon_{\text{eq}}, \epsilon_{\text{pol}}$ ) from the photocentre displacements ( $\epsilon_{\alpha}, \epsilon_{\delta}$ ). Fig. 6 shows the observed photocentre displacements ( $\epsilon_{\text{eq}}, \epsilon_{\text{pol}}$ ) with our best model (black line), which is discussed in Section 5.1. The uncertainties used for the photocentre displacements are the root-mean-square (RMS) of those of  $\phi_{\text{diff}}$  at the continuum. We used the RMS because the data reduction software of AMDLIB calculates the uncertainties from the differential piston, which is centred on the central wavelength ( $\lambda_c$ ) and is higher on the continuum than on the central line.

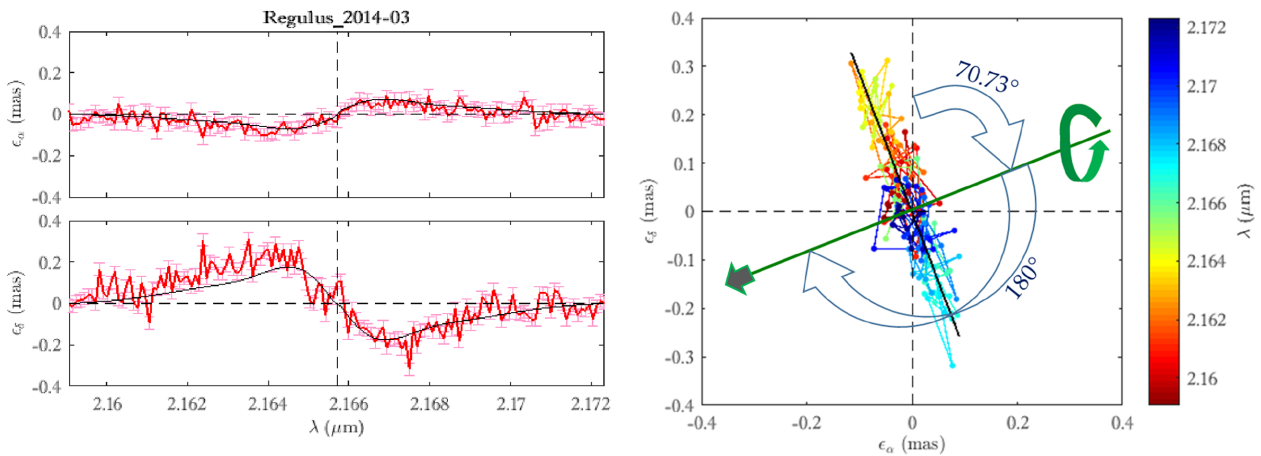


**Figure 5.** *Left:* the perpendicular right ascension and declination photocentre displacements ( $\epsilon_\alpha$ ,  $\epsilon_\delta$ ) as red thick curves for the observed data with uncertainties. The smooth thin black curves superimposed on the observations show the best-fitting  $\phi_{\text{diff}}$ , as discussed in Section 5.1. The RMS error per spectral channel has been measured in the continuum outside the spectral line and found to be  $\sim 30 \mu\text{as}$  on any projection. The two perpendicular dashed lines represent the zero-point for the photocentre displacement axis and the central wavelength ( $\lambda = 2165.7 \text{ nm}$ ) of the  $\text{Br}\gamma$  line. *Right:* the vectorial photocentre displacement on the sky. Each point represents a wavelength, as indicated by the colour bar. The black line is the fit through all points that indicates the direction of the equator and the green perpendicular line represents the rotation axis, which can be deduced directly from the angle  $PA_{\text{rot}}$ . The grey arrow with the green outline represents the apparent stellar pole. If we strictly apply the definition cited above,  $PA_{\text{rot}} = 250.73^\circ \pm 3^\circ$ .

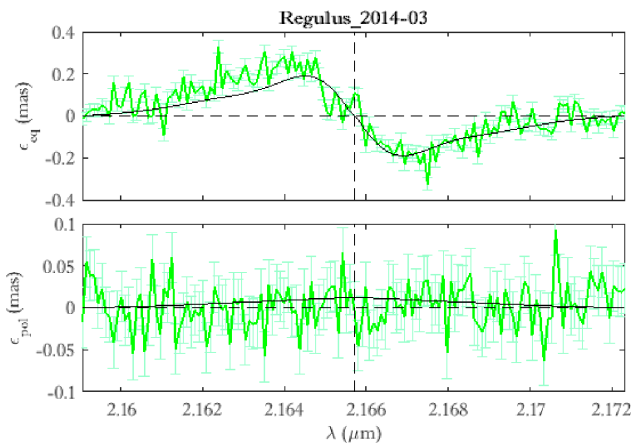


**Figure 6.** The perpendicular equatorial–polar photocentre displacements ( $\epsilon_{\text{eq}}$ ,  $\epsilon_{\text{pol}}$ ) shown as green thick curves for the observed data with uncertainties, both corresponding to the six VLTI/AMBER achieved  $(u, v)$  coverage points of Regulus, around  $\text{Br}\gamma$  at two different observing times, for each time. The smooth thin black curves superimposed on the observations are the best-fitting  $\phi_{\text{diff}}$  as discussed in Section 5.1. The two perpendicular dashed lines represent the zero-point for the photocentre displacement axis and the central wavelength ( $\lambda = 2165.7 \text{ nm}$ ) of the  $\text{Br}\gamma$  line.

## 4 MODELLING RAPID ROTATORS AND THEIR PHOTOCENTRE DISPLACEMENT

In addition to the  $PA_{\text{rot}}$  angle of the rotation vector estimate, we need a model of Regulus to interpret our measurements.

### 4.1 SCIROCCO

To interpret the  $\phi_{\text{diff}}$  observations, we use the semi-analytical model for fast rotators: Simulation Code of Interferometric-observations for ROTators and CirCumstellar Objects (SCIROCCO). This code, writ-

ten in MATLAB,<sup>2</sup> allows us to compute monochromatic intensity maps of uniformly rotating, flattened and gravity-darkened stars using a semi-analytical approach. SCIROCCO, which is a parametric description of the velocity field, intensity map and line-profile model at each point (latitude, longitude), allows us to obtain directly from the modelled specific intensity maps, on the photospheric lines, spectro-interferometric observables such as spectra and photocentres and, by using Fourier transformations, the visibility amplitudes, phases and closure phases. SCIROCCO is described in detail in Hadjara et al. (2014) and Hadjara (2015). Fig. 7 shows the modelled monochromatic intensity maps from our model for the fast-rotator study, for a given Doppler shift at three wavelengths around the  $\text{Br}\gamma$  line, adopting the stellar parameters given by our best fit, as discussed in Section 5.1, which are close to those of Che et al. (2011), i.e.  $R_{\text{eq}} = 4.16 R_\odot$ ,  $V_{\text{eq}} = 350 \text{ km s}^{-1}$ ,  $i = 86.4^\circ$  and  $PA_{\text{rot}} = 251^\circ$ . For this figure, we use the gravity-darkening coefficient estimated following the theoretical method of Espinosa Lara & Rieutord (2011) (see Section 5.1), where  $\beta \approx 0.17$ .

### 4.2 Fixed parameters

The fixed parameters that we use for our modelling are: as follows.

(i) Local velocity field.

(a) Microturbulence: any case lower than  $10 \text{ km s}^{-1}$  has no impact, as the resulting line broadening is much smaller than our spectral PSF (Point Spread Function) width of  $25 \text{ km s}^{-1}$ . We chose Regulus’s microturbulent velocity value as the solar one (i.e.  $2 \text{ km s}^{-1}$ ) by default, in order to simulate the limb-darkening effect. This choice has no effect on our final results, because Regulus is marginally resolved and in addition Regulus’s line profile is too large ( $\overline{FWHM} = 26\Delta\lambda$ ) and shallow ( $|Amp| = 0.24$ ) (see Fig. 8) to be sensitive to an accurate value of the limb-darkening coefficient in general and to the microturbulent velocity in particular.

<sup>2</sup>MATrix LABoratory

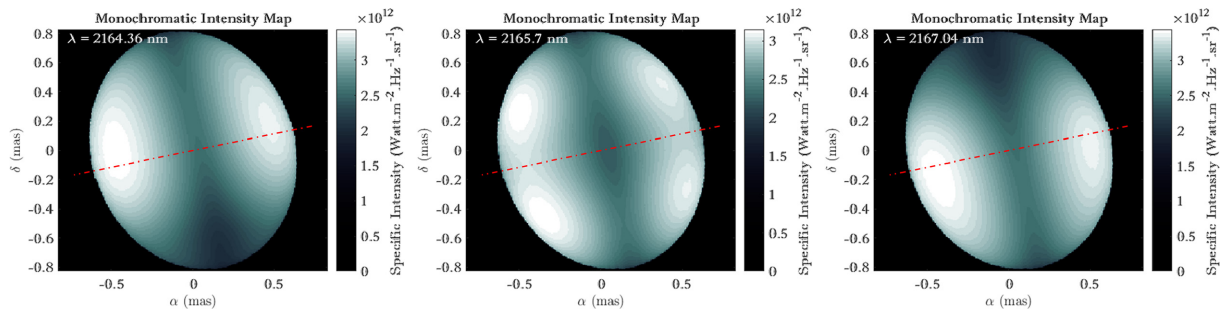


**Figure 7.** Three monochromatic intensity maps of Regulus from our simulator SCIROCCO, with physical parameters as discussed in Section 5.1, which are close to those of Che et al. (2011). The three wavelengths are in the Br $\gamma$  line and represent radial velocities of  $-185.6$ ,  $0$  and  $+185.6$  km s $^{-1}$ , from left to right. The red dashed line represents the rotation axis of the star.

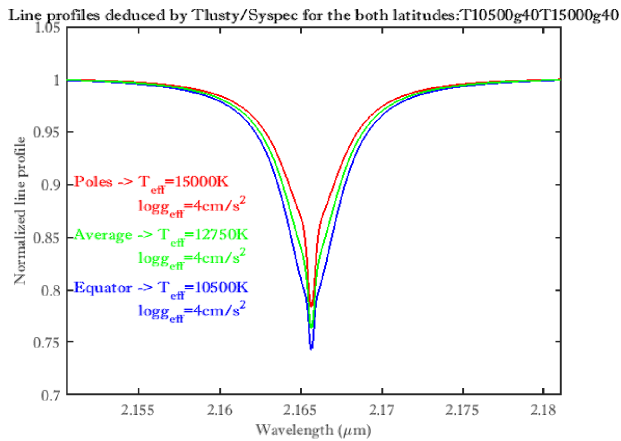


**Figure 8.** Latitude dependence of our Br $\gamma$  line profiles.

(b) Differential rotation. We can introduce it, but here we have neglected it because it introduces signatures that disappear in the noise.

(ii) Line profile. Unlike Chelli & Petrov (1995), we use a different line strength for each latitude ( $\theta$ ) of the star, fixed by the couples of latitudinal temperature and latitudinal surface gravity [ $T_\theta$ ,  $\log g_\theta$ ] from Kurucz/Syspec (synthetic spectrum) stellar atmosphere modelling.

Fig. 8 shows the local Br $\gamma$  line-profile representation for a star, from the Kurucz/Syspec model at three different latitudes: with [ $T_{\text{pol}}$ ,  $\log g_{\text{pol}}$ ] = [15 000 K, 4 cm s $^{-2}$ ] at the poles (red line), [ $T_{\text{eq}}$ ,  $\log g_{\text{eq}}$ ] = [10 500 K, 4 cm s $^{-2}$ ] at the equator (blue) and the average [12 750 K, 4 cm s $^{-2}$ ] (in green). The polar line profiles have lower amplitude than the equatorial one.

The relevant fixed parameters of our model for the rapidly rotating star Regulus are as follows.

(i) Distance  $d = 23.759 \pm 0.446$  pc, given by van Belle & von Braun (2009) from HIPPARCOS data (Perryman et al. 1997).

(ii) Mass  $M = 3.8 \pm 0.57 M_\odot$ , given by Malagnini & Morossi (1990).

(iii) Surface mean effective temperature  $\bar{T}_{\text{eff}} = 12\,500$  K, given by Malagnini & Morossi (1990). Using the spectral energy distributions (SEDs) from our model, with this  $\bar{T}_{\text{eff}}$ , we obtain the apparent magnitudes  $m_V = 1.4 \pm 0.1$  and  $m_K = 1.6 \pm 0.1$ , which are consistent, within the uncertainties, with those found in the Strasbourg

astronomical Data Center<sup>3</sup>:  $m_V = 1.40 \pm 0.05$  and  $m_K = 1.62 \pm 0.05$  (van Belle & von Braun 2009).

(iv) The limb darkening is fixed, assuming the Claret function (Claret 2000), by the following parameters:

- micro-turbulent velocity  $VT = 2$  km s $^{-1}$  (solar standard  $VT$ ),
- surface mean effective surface gravity  $\log g = 4$  cm s $^{-2}$ ,
- metallicity  $[\text{Fe}/\text{H}]^e = 0.0$  given by Che et al. (2011) and
- spectral filter in the  $K$  band.

For our model, we have selected the fixed parameters that we use in this article. In the literature, one can find slightly different values for these fixed parameters. We have checked that these changes have no impact on our interferometric measurable quantities, at our level of accuracy, nor on the parameters that we extract from a fit of our measures, as discussed in Section 5.1.

Concerning the gravity-darkening coefficient,  $\beta$  is estimated indirectly, following Espinosa Lara & Rieutord (2011), by a function of the polar and equatorial radius ratio, where

$$\beta = \frac{1}{4} - \frac{1}{3} \left(1 - \frac{R_{\text{pol}}}{R_{\text{eq}}}\right). \quad (3)$$

The formula that links  $R_{\text{eq}}$ ,  $R_{\text{pol}}$  and  $V_{\text{eq}}$  is given by Hadjara et al. (2014), Hadjara (2015) and Domiciano de Souza et al. (2002) and is shown in Appendix B.

### 4.3 Sensitivity of the photocentre displacement to $\beta$

Before describing the global fits of  $R_{\text{eq}}$ ,  $V_{\text{eq}}$ ,  $i$ ,  $PA_{\text{rot}}$  and, tentatively,  $\beta$ , we will use our model to illustrate the sensitivity of our differential photocentre measures to  $\beta$ .

Fig. 9(a) and (b) shows respectively the sensitivity of the equatorial and polar photocentre displacement to a change in the parameter  $\beta$ . With the parameters of our best model (see Section 5.1), which are close to those used by Che et al. (2011), we plot the differences between  $\epsilon(\lambda)$  for  $\beta$  and  $\epsilon(\lambda)$  for  $\beta = 0$ ; i.e.  $\Delta\epsilon(\lambda, \beta) = \epsilon(\lambda, \beta) - \epsilon(\lambda, \beta = 0)$ .

We expected a maximum signature of  $\beta$  in the rotation axis direction signal  $\Delta\epsilon_{\text{pol}}(\lambda)$ , because gravity darkening introduces a dissymmetry between the northern and southern hemispheres, if the star is not exactly equator-on. Indeed, we see a relatively regular change of the average amplitude of  $\langle \Delta\epsilon_{\text{pol}}(\lambda) \rangle_\lambda$  of the order of 8  $\mu\text{as}$  for  $\Delta\beta = 0.25$ . As  $\langle \Delta\epsilon_{\text{pol}}(\lambda) \rangle_\lambda$  can be estimated

<sup>3</sup>Available at <http://cdsweb.u-strasbg.fr/>

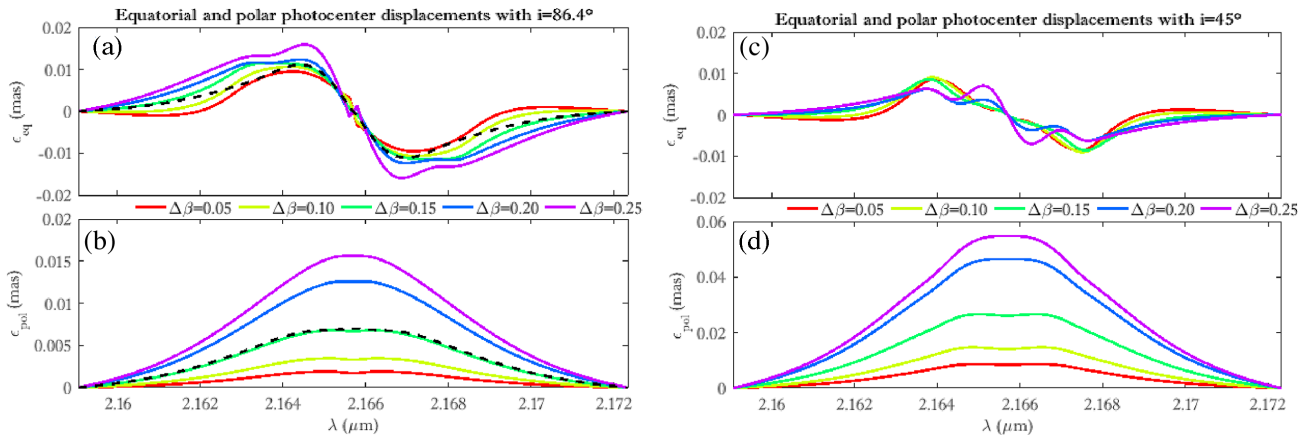


**Figure 9.** (a) and (b) Effect of changes in  $\beta$  on the equatorial and polar photocentre displacements, compared with the effect of changes in radius or inclination. In colour we plot  $\epsilon(\lambda, \beta) - \epsilon(\lambda, \beta = 0)$  for the parameters of ‘param\_set3’. The dashed dark line in the  $\epsilon_{\text{eq}}$  figure (a) shows the effect of a 6 per cent radius variation that has the same total amplitude as a  $\beta = 0.15$  variation. In the  $\epsilon_{\text{pol}}$  figure (b), the same line shows the effect of a  $8.4^\circ$  variation of the inclination  $i$  that has the same total amplitude as a  $\beta = 0.15$  variation. (c) and (d) Same as (a) and (b), but with an inclination  $i = 45^\circ$ .

with an accuracy of about  $2.5 \mu\text{as}$ , this would yield an accuracy  $\sigma_\beta \approx \frac{0.25}{8} \times 2.5 = 0.08$  if  $\beta$  is the unique unknown. However, we see that the polar photocentre displacement  $\Delta\epsilon_{\text{pol}}(\lambda)$  will not allow us to separate the effects of  $\beta$  and  $i$ : for example, a variation of  $\beta$  from 0 to 0.15 gives almost exactly the same effect on  $\Delta\epsilon(\lambda)$  as a change in inclination  $i = 8.4^\circ$ , as shown by the dashed line in Fig. 9(b) ( $\epsilon_{\text{pol}}(\lambda, \beta = 0.15, i = 78^\circ, R_{\text{eq}} = 4.16 R_\odot) - \epsilon_{\text{pol}}(\lambda, \beta = 0.15, i = 86.4^\circ, R_{\text{eq}} = 4.16 R_\odot)$ ). Surprisingly,  $\beta$  also has a strong impact on the equatorial photocentre displacement  $\Delta\epsilon_{\text{eq}}(\lambda)$ , which can be explained by the fact that the extra polar brightness enhances the weight of parts of the star with small and intermediate radial velocities with respect to the high radial velocity regions. Changes in the stellar radius have a direct influence on  $\epsilon_{\text{eq}}(\lambda) \propto R_{\text{eq}}$ . The signature of a change in radius for given  $\beta$  and of changes in  $\beta$  for a given radius are different.  $R_{\text{eq}}$  changes only the global amplitude of  $\epsilon_{\text{eq}}(\lambda)$ , while  $\beta$  changes the shape of  $\epsilon_{\text{eq}}(\lambda)$ , with, for example, a strong change in the wings of  $\epsilon_{\text{eq}}(\lambda)$  when  $\beta$  varies from 0 to 0.25. We therefore have to consider two cases. If  $\epsilon_{\text{eq}}(\lambda)$  is known, our measure of  $\langle |\epsilon_{\text{eq}}(\lambda)| \rangle > \lambda$  would yield  $\sigma_\beta \approx 0.08$ . If we consider that  $R_{\text{eq}}$  is unknown and must be estimated from our data, then the specific signature of a variation in  $\beta$  is reduced. An uncertainty of  $\sigma_R/R \leq 1.5$  per cent in  $R_{\text{eq}}$ , as in McAlister et al. (2005) and Che et al. (2011), would have almost no impact and would allow our data to constrain  $\sigma_\beta \leq 0.1$  per cent, which would be far from decisive. If we have the uncertainty  $\sigma_R/R \leq 6$  per cent, which results from our differential interferometry data alone, as we will see in the next section, the specific signature of a change in  $\beta$ , i.e. for example the difference between the variation in  $\epsilon_{\text{eq}}(\lambda)$  when  $\beta$  varies from 0.05 to 0.25, due to a 6 per cent change in radius, averaged over  $\lambda$ , is reduced to less than  $3 \mu\text{as}$ , yielding an uncertainty  $\sigma_\beta \geq 0.2$ , which is useless to constrain the modelling of the Von Zeipel effect. The dashed line in Fig. 9(a) shows the effect of angular diameter changes of 6 per cent on  $\epsilon_{\text{eq}}(\lambda)$  ( $\epsilon_{\text{eq}}(\lambda, \beta = 0.15, i = 86.4^\circ, R_{\text{eq}} = 4.41 R_\odot) - \epsilon_{\text{eq}}(\lambda, \beta = 0.15, i = 86.4^\circ, R_{\text{eq}} = 4.16 R_\odot)$ ), which has the same extrema values as the curve for a change of  $\Delta\beta = 0.15$ .

Fig. 9(c)–(d), like Fig. 9(a)–(b) but with  $i = 45^\circ$ , shows a value of  $\epsilon_{\text{eq}}$  lower in amplitude and width because of  $V_{\text{eq}} \sin i$  effect. Indeed,  $V_{\text{eq}}$  and  $i$ , which remain the same (i.e.  $350 \text{ km s}^{-1}$  and  $86.4^\circ$ ), produce an asymmetrical SED in the polar direction, which makes a non-zero  $\epsilon_{\text{pol}}$  at  $\beta = 0$  even with a 1D fixed line profile ( $[\overline{T}_{\text{eff}}, \log g_{\text{eff}}] = [12\,500 \text{ K}, 4 \text{ cm s}^{-2}]$ ).

**Table 3.** Physical characteristics [ $T_{\text{eff}}, \log g$ ], from equator to pole, of the line profile corresponding to each  $\beta$ .

$\beta$	Range of $\beta$	Real [ $T_{\text{eff}}, \log g$ ] (K, $\text{cm s}^{-2}$ )	Kurucz/Tlusty [ $T_{\text{eff}}, \log g$ ] (K, $\text{cm s}^{-2}$ )
0.00	–	[12 500, 4.0] [11 946, 3.78]	[12 500, 4.0] [12 000, 4.0]
0.05	0.05–0.07	to [13 054, 4.04] [11 367, 3.78]	to [13 000, 4.0] [11 500, 4.0]
0.10	0.08–0.12	to [13 633, 4.04] [10 762, 3.78]	to [14 000, 4.0] [10 750, 4.0]
0.15	0.13–0.17	to [14 238, 4.04] [10 130, 3.78]	to [14 000, 4.0] [10 000, 4.0]
0.20	0.18–0.22	to [14 870, 4.04] [9 471, 3.78]	to [15 000, 4.0] [9 500, 4.0]
0.25	0.23–0.25	to [15 529, 4.04]	to [15 000, 4.0]

in the same conditions. Indeed, between  $i = 90^\circ$  and  $i = 45^\circ$ , the  $\epsilon_{\text{pol}}$  amplitude wins a factor of  $\sim 3$  and the impact of  $\beta$  is more distinguishable, where  $\epsilon_{\text{pol}}$  is larger than  $\sigma_\epsilon = 30 \mu\text{as}$ , when  $\epsilon_{\text{pol}}$  is drowned in its noise for  $i = 90^\circ$  (Fig. 6). What this means is that the  $\beta$  estimation method using the photocentre displacements we propose here is supposed to work better with fast rotators with inclination around of  $45^\circ$ , despite their angular resolution and/or their SNR.

The physical characteristics [ $T_{\text{eff}}, \log g$ ], from equator to pole, of the line profiles corresponding to each  $\beta$  used in this article are summarized in Table 3.

Note also that  $\epsilon_{\text{pol}}$  is not zero at  $\beta = 0$ , because of the  $V_{\text{eq}} \sin i$  effect. Indeed,  $V_{\text{eq}}$  and  $i$ , which remain the same (i.e.  $350 \text{ km s}^{-1}$  and  $86.4^\circ$ ), produce an asymmetrical SED in the polar direction, which makes a non-zero  $\epsilon_{\text{pol}}$  at  $\beta = 0$  even with a 1D fixed line profile ( $[\overline{T}_{\text{eff}}, \log g_{\text{eff}}] = [12\,500 \text{ K}, 4 \text{ cm s}^{-2}]$ ).

## 5 FITTING THE FUNDAMENTAL PARAMETERS OF REGULUS

### 5.1 $\chi^2$ minimization

In order to deduce the best parameters fitting differential phase data, we perform a  $\chi^2$  minimization<sup>4</sup> for the  $\phi_{\text{diff}}$  data. We use the corresponding photocentre displacements ( $\epsilon_{\text{eq}}$ ,  $\epsilon_{\text{pol}}$ ) here. The uncertainties used in this minimization are those of  $\phi_{\text{diff}}$ .

We use four model-fitting parameter sets ('param\_set'). The free parameters are  $R_{\text{eq}}$  (equatorial radius),  $V_{\text{eq}}$  (equatorial velocity),  $i$  (inclination angle) and  $PA_{\text{rot}}$  (rotation-axis position angle). Because  $PA_{\text{rot}}$  is determined well by the method of the photocentre displacement slope that we showed in Section 3, we start with model-fitting to deduce the three free parameters:  $R_{\text{eq}}$ ,  $V_{\text{eq}}$  and  $i$  (with  $PA_{\text{rot}}$  fixed). We also checked the real independence of  $PA_{\text{rot}}$  and the best solution, using a model fitting with four free parameters:  $R_{\text{eq}}$ ,  $V_{\text{eq}}$ ,  $i$  and  $PA_{\text{rot}}$ .

In our study, where we change the value of  $\beta$  (fixed/indirectly estimated by equation 3), the couples equatorial–polar effective temperature and effective surface gravity, [ $T_{\text{eq}}$ ,  $\log g_{\text{eq}}$ ] and [ $T_{\text{pol}}$ ,  $\log g_{\text{pol}}$ ], required for constructing our three-dimensional (3D) line profile are deduced by running the  $\chi^2$  fitting of our model once on the observation data, with a fixed line profile [ $T_{\text{eff}}$ ,  $\log g_{\text{eff}}$ ].

Parameter set 1 ('param\_set1') represents the most complete SCIROCCO modelling of Regulus for three free parameters  $R_{\text{eq}}$ ,  $V_{\text{eq}}$  and  $i$  (with  $PA_{\text{rot}}$  fixed), gravity-darkening coefficient  $\beta$  theoretically estimated from equation (3), an analytic 3D Kurucz/Synspec line profile and latitudinal limb darkening (depending on  $\theta$ ). Parameter set 2 ('param\_set2') is similar to 'param\_set1' but with  $\beta$  fixed to the value of 0.25.

Parameter set 3 ('param\_set3') represents the most complete SCIROCCO modelling of Regulus for four free parameters  $R_{\text{eq}}$ ,  $V_{\text{eq}}$ ,  $i$  and  $PA_{\text{rot}}$ . Parameter set 4 ('param\_set4') is similar to 'param\_set3' but with  $\beta$  fixed to 0.25.

We show here only the results of the most complete model ('param\_set3'), because we found that results for all four parameter sets are similar within the uncertainties. All the best-fitting values of all parameter sets are summarized in Table C1 in Appendix C. The similarity of the  $PA_{\text{rot}}$  results between parameter sets 3 and 4 and parameter sets 1 and 2 confirms the independence of  $PA_{\text{rot}}$  and the similarity of the results between all parameter sets (with respect to the uncertainties), where  $\beta$  is fixed and deduced indirectly, confirms the difficulty in constraining  $\beta$  with our current data.

Table 4 summarizes the results of 'param\_set3', which has been chosen as the reference 'param\_set' model-fitting with the MCMC uncertainties (the justification for this choice is well explained in Section 5.2), where  $R_{\text{eq}} = 4.16 \pm 0.24 R_{\odot}$ ,  $V_{\text{eq}} = 350 \pm 22 \text{ km s}^{-1}$ ,  $i = 86.4 \pm 6.3^{\circ}$  and  $PA_{\text{rot}} = 251 \pm 2^{\circ}$ . The comparison of our results with those found in the literature (in Table 4) confirms that the use of differential phases alone for the  $\chi^2$  minimization is largely sufficient to constrain the fundamental stellar parameters, as has been done in the past for Achernar by Domiciano de Souza et al. (2012) and for Achernar, Altair,  $\delta$  Aquilae & Fomalhaut by Hadjara et al. (2014).

Figs 5 (left panel) and 6 (see Section 3) show the best fit to both photocentre displacements ( $\epsilon_{\text{eq}}$ ,  $\epsilon_{\text{pol}}$ ) and ( $\epsilon_{\alpha}$ ,  $\epsilon_{\delta}$ ) obtained with 'param\_set3'. In Fig. 6, we observe that the equatorial photocentre

displacement  $\epsilon_{\text{eq}}$  is more important than the polar one  $\epsilon_{\text{pol}}$ . Indeed, the rotation is in the equatorial direction and the asymmetry in the modelling  $\epsilon_{\text{pol}}$ , which is quasi-flat, corresponds to the combination of the inclination angle  $i = 86.4^{\circ}$  and the Von Zeipel effect. (This last produces a small asymmetry, around the Br $\gamma$  line, in  $\epsilon_{\text{pol}}$ . This asymmetry is obvious in the modelling  $\epsilon_{\text{pol}}$  and buried in the noise of the observations.) Whereas  $\epsilon_{\text{eq}}$  starts at zero for the first wavelength, increasing before going to zero at the centre of the Br $\gamma$  line, becoming negative after that and continuing to decrease before increasing to zero again at the last wavelength,  $\epsilon_{\text{pol}}$  starts from zero and increases until the centre of the Br $\gamma$  line before decreasing again to zero at the last wavelength.

### 5.2 MCMC verification

In order to check the results obtained with the  $\chi^2$  minimization method and study the coupling of the free parameters between them, we apply the MCMC technique, following the Delayed Rejection and Adaptive Metropolis samplers (DRAM) method (Haario et al. 2006). We start around the best four free parameters that we obtained with the  $\chi^2$  minimization method for 'param\_set3' ( $R_{\text{eq}} = 4 R_{\odot}$ ,  $V_{\text{eq}} = 300 \text{ km s}^{-1}$ ,  $i = 85^{\circ}$  and  $PA_{\text{rot}} = 250^{\circ}$ ). The upper and lower bounds were determined as follows:  $2 R_{\odot} \leq R_{\text{eq}} \leq 5 R_{\odot}$ ,  $250 \text{ km s}^{-1} \leq V_{\text{eq}} < 450$ ,  $45^{\circ} \leq i \leq 135^{\circ}$  and  $200^{\circ} \leq PA_{\text{rot}} \leq 300^{\circ}$ .

Because of the stochasticity of the MCMC method, which needs an important number of iterations, we were able to constrain all the free parameters except  $V_{\text{eq}}$ , which we systematically found to be far above the critical velocity. To fix this problem, we deduce the MCMC best parameters by fitting the differential phase and the spectrum data together.

MCMC explores the full posterior distribution using a set of random simulations of SCIROCCO with a frequency of adaptation. The result of the simulations is used for the next step, in order to optimize the maximum likelihood. We run MCMC with 600 simulations and 50 points of adaptation frequency. We perform three successive runs, starting from the values of the previous run, because we started from non-optimized values and the chain needs some time to find the location of the posterior. At the last run, all the simulations are around the maximum likelihood and their average represents the best solution well, while the standard deviation provides the uncertainties. Fig. A1 (in Appendix A) shows, in addition to the covariance matrix, pairs of parameters with their histogram. The results of this method are close to those of the  $\chi^2$  minimization. The uncertainties of the parameters estimated by the LM algorithm are  $\approx 3$  per cent for  $R_{\text{eq}}$ ,  $\approx 5$  per cent for  $V_{\text{eq}}$ ,  $\approx 2$  per cent for  $i$  and  $\approx 4$  per cent for  $PA_{\text{rot}}$ , while the MCMC uncertainties are  $\approx 5$  per cent for  $R_{\text{eq}}$  and  $V_{\text{eq}}$ ,  $\approx 7$  per cent for  $i$  and  $\approx 8$  per cent for  $PA_{\text{rot}}$ . The uncertainties of all the free parameters, except for  $PA_{\text{rot}}$ , are much larger in the MCMC method than in the  $\chi^2$  minimization (between two and five times), because the MCMC uncertainties take into account the coupling between the free parameters. Thus, the MCMC method is supposed to find the real errors considered in this article (Table 4).

### 5.3 Fitting results

Our results, which come from the photocentre displacements, have relatively greater uncertainties than the results that come from classical long-baseline and large-band interferometry, except for  $V_{\text{eq}}$ , because of the high spectral resolution mode used by AMBER, and  $PA_{\text{rot}}$  (with the MCMC method). We confirmed the same value of  $PA_{\text{rot}}$  with three different methods – directly, with  $\chi^2$  minimization

<sup>4</sup>The description of this method was explained well in Hadjara et al. (2014)

**Table 4.** Parameters estimated from a Levenberg–Marquardt fit and their uncertainties from the MCMC fit.

Parameters	Regulus		
Best-fitting parameter	In the literature		param_set 3 with MCMC uncertainties
Equatorial radius $R_{\text{eq}}$	$4.16 \pm 0.08 R_{\odot}^1$	$4.21^{+0.07}_{-0.06} R_{\odot}^2$	$4.16 \pm 0.24 R_{\odot}^3$
Equatorial rotation velocity $V_{\text{eq}}$	$317^{+3}_{-85} \text{ km s}^{-1}$	$337^{+22}_{-33} \text{ km s}^{-1}$	$350 \pm 22 \text{ km s}^{-1}$
Rotation-axis inclination angle $i$	$90^{+0}_{-15} \text{ }^\circ$	$86.3^{+1}_{-1.6} \text{ }^\circ$	$86.4 \pm 6.3^\circ$
Rotation-axis position angle $PA_{\text{rot}}$	$265.5 \pm 2.8^\circ$	$258^{+2}_{-1} \text{ }^\circ$	$251 \pm 2^\circ$
No. of free parameters	5 <sup>1</sup>	6 <sup>2</sup>	4
$\chi^2$	3.35 <sup>1</sup>	1.32 <sup>2</sup>	2.71
<b>Fixed parameter</b>			<b>Value</b>
Distance $d$	$23.5 \pm 0.4 \text{ pc}^1$	$24.31 \pm 0.24 \text{ pc}^2$	$23.759 \pm 0.446 \text{ pc}^3$
Mass $M$	$3.39 \pm 0.24 M_{\odot}^1$	$3.66^{+0.79}_{-0.28} M_{\odot}^2$	$3.8 \pm 0.57 M_{\odot}^4$
Surface mean effective temperature $\bar{T}_{\text{eff}}$	12 250 K	12 080 K	$12\,500 \text{ K}^4$
Gravity-darkening coefficient $\beta$	Free		Estimated
<b>Limb-darkening parameters</b>			
Turbulent velocity $V_T$	–		$2 \text{ km s}^{-1}$
$\log g$	$\log g_{\text{eff}} = 3.5 \text{ cm s}^{-2}$ <sup>1</sup>		$4 \text{ cm s}^{-2}$
Claret $T_{\text{eff}}$	–		10 500–15 000 K
Metallicity [Fe/H] <sup>e</sup>	–	$0.0^2$	0.0
Spectral filter	–		K
<b>Line profile</b>			
Kind	–		Kurucz/Synspec
Physical characteristics [ $T_{\text{eff}}$ , $\log g$ ]	–		[10 500 K, $4 \text{ cm s}^{-2}$ ] to [15 000 K, $4 \text{ cm s}^{-2}$ ]
<b>Derived parameter</b>			<b>Value</b>
Equatorial angular diameter $\mathcal{D}_{\text{eq}}$	$1.65 \pm 0.02 \text{ mas}$	$1.61^{+0.03}_{-0.02} \text{ mas}$	$1.63 \pm 0.09 \text{ mas}$
Equatorial-to-polar radii $R_{\text{eq}}/R_{\text{pol}}$	$1.32 \pm 0.04$	$1.31^{+0.05}_{-0.04}$	$1.35 \pm 0.08$
Critical radius $R_{\text{crit}}$	$4.72 \pm 0.04 R_{\odot}$	$4.83^{+0.05}_{-0.04} R_{\odot}$	$4.61 \pm 0.53 R_{\odot}$
Critical equatorial rotation velocity $V_{\text{crit}}$	$369^{+14}_{-67} \text{ km s}^{-1}$	$380^{+85}_{-32} \text{ km s}^{-1}$	$396 \pm 46 \text{ km s}^{-1}$
$V_{\text{eq}} \sin i$	$317 \pm 3 \text{ km s}^{-1}$	$336^{+16}_{-24} \text{ km s}^{-1}$	$349 \pm 60 \text{ km s}^{-1}$
$V_{\text{eq}}/V_{\text{crit}}$	$0.86 \pm 0.03$	$0.89^{+0.25}_{-0.16}$	$0.88 \pm 0.05$
$\beta$	$0.25 \pm 0.11$	$0.188^{+0.012}_{-0.029}$	$0.165 \pm 0.009^5$
Polar effective temperature $T_{\text{pol}}$	$15\,400 \pm 1\,400 \text{ K}$	$14\,520^{+550}_{-690} \text{ K}$	$14\,419 \pm 832 \text{ K}$
Equatorial effective temperature $T_{\text{eq}}$	$10\,314 \pm 1\,000 \text{ K}$	$11\,010^{+420}_{-520} \text{ K}$	$10\,581 \pm 612 \text{ K}$
Luminosity $\log LL_{\odot}$	$2.540 \pm 0.043$	$2.533^{+0.033}_{-0.037}$	$2.461 \pm 0.070$

Notes:

<sup>1</sup> McAlister et al. (2005);<sup>2</sup> Che et al. (2011);<sup>3</sup> Perryman et al. (1997);<sup>4</sup> Malagnini & Morossi (1990);<sup>5</sup> Theoretical estimate of  $\beta$  from Espinosa Lara & Rieutord (2011).**Table 5.** Limiting and achieved accuracy for the parameter  $\beta$  of Regulus with our data. The best possible accuracy is given for the estimation of a parameter when we assume that all other parameters are known.

Parameter	Best possible accuracy from $\epsilon(\lambda)$ only	Accuracy from MCMC fit of $\epsilon(\lambda)$ and $s(\lambda)$
$\beta$ with $\sigma_{R_{\text{eq}}}$	0.08	n.a.
$\beta$ with $\sigma_{R_{\text{eq}}}/R_{\text{eq}} = 5.7$	0.3	n.a.

and with the MCMC method – with good accuracy and we estimate that our  $PA_{\text{rot}}$  is fairly reliable.

All our results confirm what was found before in the literature (McAlister et al. 2005; Che et al. 2011), except for the equatorial velocity  $V_{\text{eq}}$ , which is  $\approx 10$  per cent higher. Despite this important difference, we argue that our result of  $V_{\text{eq}}$  is the fairest, because it was deduced from differential phases (photocentre displacement),

which are directly related to  $V_{\text{eq}}$ . In addition, our result has been validated by two different minimization methods.

The parameters that are sensitive and are further away from a hypothetical case without the Von Zeipel effect are  $V_{\text{eq}}$  and  $i$ . The first parameter that appears with the Von Zeipel effect is the inclination angle  $i$ , which gives the true rotation  $V_{\text{eq}}$  (Maeder & Peytremann 1972). The second parameter is the rotation-axis position angle of our star ( $PA_{\text{rot}}$ ), which we can deduce, as seen previously, directly from the 2D observed photocentres (see Section 3). The value adopted for  $PA_{\text{rot}}$  of  $251^\circ$  (west–east rotation direction) is in agreement with the values given by the  $\chi^2$ /MCMC fitting ( $PA_{\text{rot}} = 251.11 \pm 1.82^\circ$ ).

The gravity-darkening coefficient  $\beta$  is very important in the physics of rotating stars.  $\beta = 0.25$  is a standard value for stars with radiative envelopes in hydrostatic equilibrium (von Zeipel 1924a,b). We consider it as a first approximation of the surface distribution of the radiative flux with the hypothesis of conservative laws of rotation (centrifugal force obtained from a potential). For stars with convec-

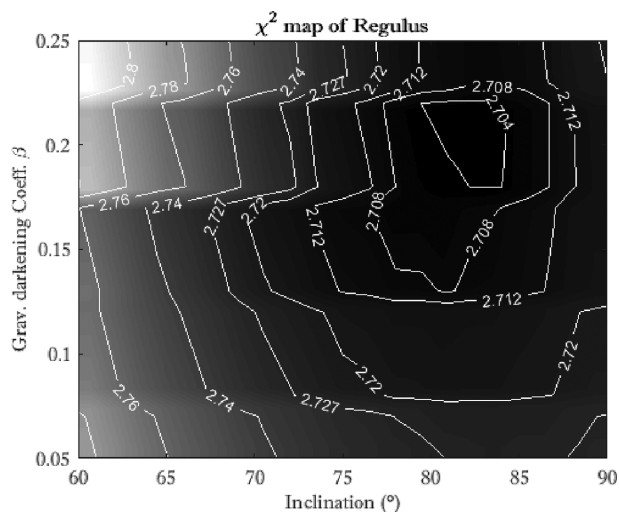


**Figure 10.**  $\chi^2$  map of Regulus that shows the degeneracy between the stellar parameters  $i$  and  $\beta$ . The numerical solid white contours represent the  $\chi^2$  value. This combination favours values of  $0.14 \leq \beta \leq 0.22$  and  $77^\circ \leq i \leq 87^\circ$  with a  $\chi^2$  value of 2.71.

tive layers, Lucy (1967) showed that  $\beta \approx 0.08$  and Che et al. (2011) recommend adopting  $\beta \approx 0.19$  for the modelling of radiative stars in rotation. The insufficient spatial resolution of our observations prevented us from determining the gravity-darkening coefficient  $\beta$  of Regulus directly, by setting it as a free parameter in  $\chi^2$  minimization. Our attempts to constrain  $\beta$  using this method produced physically meaningless results, which can be explained by taking into account the degeneracy of the solution (see Section 6). On the other hand, we can estimate it theoretically according to the method of Espinosa Lara & Rieutord (2011), who propose using a  $\beta$ -value adapted to each rotator according to its velocity. They adopted for Regulus a value of  $\beta$  between 0.158 and 0.198 from the results of Che et al. (2011), while, using the Espinosa Lara & Rieutord (2011) method with our  $R_{\text{pol}}$  and  $R_{\text{eq}}$  results (from Table 4), we deduce that  $\beta$  is  $\sim 0.17 \pm 0.1$ .

## 6 DISCUSSION

We have used our SCIRROCCO modelling tool to estimate the effect on  $\epsilon(\lambda)$  of the rotation-axis position angle and inclination, equatorial radius, equatorial velocity and gravitational darkening parameter  $\beta$ . We have shown that the position angle of the rotation vector can be measured, in direction and orientation, independently from the other parameters, as it is the oriented axis of symmetry of the 2D track of  $\epsilon(\lambda)$  for all possible values of the other parameters. We have computed the limits of accuracy of  $\beta$  that we could achieve with our quality of data and these numbers are summarized in Table 5.

Our estimates show that our SNR is insufficient to give a significant direct constraint on  $\beta$  from a fit of our data.

Because of the particular ‘edge-on’ position of Regulus and the symmetry of the equator-on orientation,  $(\beta, i)$  should be degenerate (Che et al. 2011). Therefore, from the Regulus 2D  $\chi^2$  map with ‘param\_set3’ and for  $0.05 \leq \beta \leq 0.25$  and  $60^\circ \leq i \leq 90^\circ$ , we deduced the probability space that shows the degeneracy between stellar parameters  $i$  versus  $\beta$ .

From Fig. 10, where we show the Regulus  $\chi^2$  map  $(\beta, i)$ , we

can observe an important degeneracy of solution for  $\beta$  and  $i$  using our model SCIRROCCO. This figure shows an enlarged contour of  $\chi^2$ , implying an important correlation between  $\beta$  and  $i$ . The value of  $\chi^2$  is almost the same (between 2.704 and 2.727) in a large zone, where  $70^\circ \leq i \leq 90^\circ$  and  $0.05 \leq \beta \leq 0.25$ , which makes the accurate determination of  $\beta$  very difficult. The third numerical white solid contour shows the  $\chi^2$  zone with a value of 2.712. Our best model-fitting result from ‘param\_set3’ ( $i = 86.4 \pm 6.3^\circ$  and  $\beta = 0.17 \pm 0.01$ ) is in this area too. The degeneracy  $(\beta, i)$  in our study is more important than that of Che et al. (2011), because of the angular resolution quality of both observations.

It might be possible to improve the constraints by combining our data with the results or, better, the individual measures from previous techniques. For example, we could use the angular diameter from previous interferometric measures and better spectra of Regulus (the SNR of the AMBER spectrum is quite poor) for better constraints on the inclination and even  $\beta$ . With an accuracy on the radius  $\sigma_{R_{\text{eq}}}/R_{\text{eq}} = 1.5$  per cent as in the McAlister et al. (2005) and Che et al. (2011) measures, our data would yield  $\sigma_\beta \approx 0.15$  and a gain in SNR  $\sim 3$  would be enough to achieve  $\sigma_\beta \approx 0.05$ . For high spectral resolution differential phase measurements, the accuracy at the photocentre increases proportionally with angular diameter, aperture size and baseline length (Petrov 1989). With larger apertures (the Unit Telescopes) or larger baselines and shorter wavelengths (CHARA in the visible with a high spectral resolution instrument) and even with smaller and fainter sources, such a gain in SNR seems quite accessible. A source with an inclination closer to  $45^\circ$  would also provide a larger signal in the polar direction (Fig. 9d). This opens excellent perspectives for future observations of rapid rotators with high spectral resolution differential interferometry.

From the Be catalogue of Frémat et al. (2005), we found  $\sim 50$  per cent of stars with  $m_V = 2.33\text{--}7.3$ , which corresponds to the selection criteria  $30 \leq i \leq 60$  and  $v/v_c \leq 70$  per cent, which could be studied by the method that we propose in this article.

## 7 CONCLUSIONS

We have presented differential interferometry data obtained on the rapid rotator Regulus with the high spectral resolution mode of the VLTI instrument AMBER. We have seen that, for  $K$ -band observations with VLTI baselines, this target is much smaller than the angular resolution ( $\lambda/B$ ) and is not resolved enough for the Rayleigh criteria and for imaging, as all closure phases are equal to zero. It is also not resolved enough for oblateness estimations from absolute visibility measurements, because the visibility is equal to 1 within the error bars for baselines close to the polar direction and we can only give an upper limit for the polar diameter that is smaller than the equatorial diameter. We have therefore concentrated on interpretation and model fitting of the differential phases that, for this source much smaller than the standard resolution limit  $\lambda/B$ , can all be reduced to the vectorial displacement of the photocentre  $\epsilon(\lambda)$  in the spectral channel  $\lambda$  with respect to the photocentre of the target in the continuum. Our data, corresponding to  $\sim 30$  min ( $\sim 25$  min for the night 2014 March 10 and  $\sim 40$  min for the night 2014 March 12) of open shutter observations on Regulus, yield a typical error per spectral measure (half spectral channel) of  $30 \mu\text{as}$  for both the  $\alpha$  and  $\delta$  components of the vector  $\epsilon(\lambda)$  and its polar and equatorial components obtained after direct computation of the rotation-axis position angle.

We have basically confirmed the previous interferometric and spectroscopic determinations of the fundamental parameters of Reg-

ulus, with our quite different data set and different constraints on the physical parameters. Our  $350 \pm 22 \text{ km s}^{-1}$  velocity measurement is compatible within errors with the one used by Che et al. (2011), but is significantly higher than earlier estimates. This leads to a rotation at 88 per cent of the critical velocity. Our  $PA_{\text{rot}}$  measurement of  $251 \pm 2^\circ$ , which is only deduced from the vectorial photocentre ( $\phi_{\text{diff}}$ ), is little different from that deduced from squared visibilities, closure phase and triple amplitudes of CHARA/MIRC by Che et al. (2011). The vectorial photocentre is very sensitive to the  $PA_{\text{rot}}$  parameter.

We do not claim at all that our values of  $\beta$  are conclusive, because we are not able to constrain the gravity-darkening coefficient from our current data, which are relatively noisy with marginal angular resolution, and cannot forget the fact that Regulus is a edge-on star.

Despite the fact that the star was marginally resolved with our observations, we were able, for the first time, to constrain independently (from  $\epsilon_\alpha$  and  $\epsilon_\delta$ ) several fundamental stellar parameters, such as  $PA_{\text{rot}}$ , with low uncertainties. This method can be applied to stars that can only be marginally resolved or are not angularly resolved at all, because of available baseline lengths, and especially to rotators with inclination angles around  $45^\circ$  and a good SNR.

## ACKNOWLEDGEMENTS

This article was based on observations performed at the European Southern Observatory, Chile under ESO AMBER Visitor mode program IDs 092.D-0342. This research made use of the SIMBAD database, operated at the CDS, Strasbourg, France, and of the NASA Astrophysics Data System Abstract Service. The author, M. Hadjara, acknowledges support from the scientific French association PSTJ<sup>5</sup> for its official host agreement, the Lagrange and OCA for computer server support. This research made use of the Jean-Marie Mariotti Center *searchCal* service<sup>6</sup> codeveloped by Lagrange and IPAG, and of the CDS Astronomical Databases SIMBAD and VIZIER.<sup>7</sup> This research made use of the AMBER data reduction package of the Jean-Marie Mariotti Center.<sup>8</sup> Special thanks go to the project's grant ALMA-CONICYT No. 31150002 and the PI, Keiichi Ohnaka, who supported this work.

## REFERENCES

Anderson E., Francis C., 2012, *Astron. Lett.*, 38, 331  
 Beckers J. M., 1982, *Optica Acta*, 29, 361  
 Che X. et al., 2011, *ApJ*, 732, 68  
 Chelli A., Petrov R. G., 1995, *A&AS*, 109, 401  
 Chelli A., Utrera O. H., Duvert G., 2009, *A&A*, 502, 705  
 Claret A., 2000, *A&A*, 363, 1081  
 Demarque P., Woo J.-H., Kim Y.-C., Yi S. K., 2004, *ApJS*, 155, 667  
 Domiciano de Souza A. et al., 2012, *A&A*, 545, A130  
 Domiciano de Souza A., Vakili F., Jankov S., Janot-Pacheco E., Abe L., 2002, *A&A*, 393, 345  
 Domiciano de Souza A., Kervella P., Jankov S., Abe L., Vakili F., di Folco E., Paresce F., 2003, *A&A*, 407, L47

Espinosa Lara F., Rieutord M., 2011, *A&A*, 533, A43  
 Frémat Y., Zorec J., Hubert A.-M., Floquet M., 2005, *A&A*, 440, 305  
 Gerbaldi M., Faraggiana R., Balin N., 2001, *A&A*, 379, 162  
 Gies D. R. et al., 2008, *ApJ*, 682, L117  
 Gray R. O., Corbally C. J., Garrison R. F., McFadden M. T., Robinson P. E., 2003, *AJ*, 126, 2048  
 Haario H. M. L., Mira A., Saksman E., 2006, *Statistics and Computing*, 16, 339  
 Hadjara M. et al., 2014, *A&A*, 569, A45  
 Hadjara M., 2015, PhD thesis, Université de Sophia Antipolis, 28 Avenue Valrose, 06100 Nice, France.  
 Hanbury Brown R., Davis J., Allen L. R., 1974, *MNRAS*, 167, 121  
 Iorio L., 2008, *Ap&SS*, 318, 51  
 Jankov S., 2011, *Serbian Astron. J.*, 183, 1  
 Jankov S., Vakili F., Domiciano de Souza A., Jr., Janot-Pacheco E., 2001, *A&A*, 377, 721  
 Johnson H. L., Morgan W. W., 1953, *ApJ*, 117, 313  
 Labeyrie A., 1975, *ApJ*, 196, L71  
 Lachaume R., 2003, *A&A*, 400, 795  
 Lagarde S., 1994, PhD thesis, Université de Sophia Antipolis, 28 Avenue Valrose, 06100 Nice, France  
 Le Bouquin J.-B., Absil O., Benisty M., Massi F., Mérand A., Stefl S., 2009, *A&A*, 498, L41  
 Lucy L. B., 1967, *Z. Astrophys.*, 65, 89  
 Maeder A., Meynet G., 1989, *A&A*, 210, 155  
 Maeder A., Peytreman E., 1972, *A&A*, 21, 279  
 Malagnini M. L., Morossi C., 1990, *A&AS*, 85, 1015  
 Mason B. D., Wycoff G. L., Hartkopf W. I., Douglass G. G., Worley C. E., 2001, *AJ*, 122, 3466  
 McAlister H. A. et al., 2005, *ApJ*, 628, 439  
 Meilland A. et al., 2007, *A&A*, 464, 59  
 Mérand A., Patru F., Berger J.-P., Percheron I., Poupar S., 2012, in *Optical and Infrared Interferometry III*. p. 84451K  
 Millour F., Vannier M., Petrov R. G., Chesneau O., Dessart L., Stee P., 2006, in *Carbillet M., Ferrari A., Aime C., eds, EAS Publications Series Vol. 22, EAS Publications Series*. p. 379–388  
 Millour F., Meilland A., Chesneau O., Stee P., Kanaan S., Petrov R., Mourard D., Kraus S., 2011, *A&A*, 526, A107  
 Monnier J. D. et al., 2007, *Science*, 317, 342  
 Perryman M. A. C. et al., 1997, *A&A*, 323, L49  
 Petrov R. G. et al., 2007, *A&A*, 464, 1  
 Petrov R. G., 1988, in *Merkle F., ed., European Southern Observatory Conference and Workshop Proceedings Vol. 29, European Southern Observatory Conference and Workshop Proceedings*. p. 235–248  
 Petrov R. G., 1989, in *Alloin D. M., Mariotti J.-M., eds, NATO ASIC Proc. 274: Diffraction-Limited Imaging with Very Large Telescopes*. p. 249  
 Petrov R. G., Lagarde S., 1992, in *McAlister H. A., Hartkopf W. I., eds, Astronomical Society of the Pacific Conference Series Vol. 32, IAU Colloq. 135: Complementary Approaches to Double and Multiple Star Research*. p. 477  
 Rappaport S., Podsiadlowski P., Horev I., 2009, *ApJ*, 698, 666  
 Slettebak A., 1954, *ApJ*, 119, 146  
 Tatulli E. et al., 2007, *A&A*, 464, 29  
 van Belle G. T., 2012, *A&A Rev.*, 20, 51  
 van Belle G. T., von Braun K., 2009, *ApJ*, 694, 1085  
 van Leeuwen F., ed., 2007, *Hipparcos, the New Reduction of the Raw Data, Astrophysics and Space Science Library Vol. 350*  
 von Zeipel H., 1924a, *MNRAS*, 84, 665  
 von Zeipel H., 1924b, *MNRAS*, 84, 684  
 Whelan E. T., Huélamo N., Alcalá J. M., Lillo-Box J., Bouy H., Barrado D., Bouvier J., Merín B., 2015, *A&A*, 579, A48  
 Yi S., Demarque P., Kim Y.-C., Lee Y.-W., Ree C. H., Lejeune T., Barnes S., 2001, *ApJS*, 136, 417  
 Yi S. K., Kim Y.-C., Demarque P., 2003, *ApJS*, 144, 259  
 Zhao M. et al., 2009, *ApJ*, 701, 209

<sup>5</sup><http://www.pstj.fr/>

<sup>6</sup>Available at <http://www.jmmc.fr/searchcal>

<sup>7</sup>Available at <http://cdsweb.u-strasbg.fr/>

<sup>8</sup>Available at <http://www.jmmc.fr/amberdrs>

## APPENDIX A: MCMC PLOTS AND STUDY OF CORRELATIONS

Fig. A1 shows the covariance matrix: pairs of parameters, with their histogram, that were obtained by the MCMC method.

At first sight, among all four parameters, only the equatorial velocity  $V_{\text{eq}}$  and the inclination  $i$  are strongly correlated, because they are both correlated with  $V_{\text{eq}} \sin i$ . However, quantitatively and using the correlation coefficient  $\rho$ , which is defined for two scalar quantities  $A$  and  $B$  as  $\rho(A, B) = \text{cov}(A, B) / (\sigma_A \sigma_B)$ , where  $\text{cov}$  is the covariance and  $\sigma$  the standard deviation, we found, in descending order,  $\rho(R_{\text{eq}}, i) = 0.4247$ ,  $\rho(R_{\text{eq}}, PA_{\text{rot}}) = -0.3379$ ,  $\rho(i, PA_{\text{rot}}) = -0.3228$ ,  $\rho(R_{\text{eq}}, V_{\text{eq}}) = -0.3044$ ,  $\rho(V_{\text{eq}}, i) = 0.1124$  and  $\rho(V_{\text{eq}}, PA_{\text{rot}}) = -0.0730$ . When  $\rho = 1$  it means full correlation, while  $\rho = 0$  means no correlation. When  $\rho > 0$ , the correlation is proportional ( $A$  and  $B$  increase or decrease together), and when  $\rho < 0$  the correlation is inversely proportional ( $A$  increases when  $B$  decreases and vice versa), e.g. the case of  $R_{\text{eq}}$  and  $V_{\text{eq}}$ , because of angular momentum conservation. Note also that the correlation coefficients of all our free MCMC parameters are symmetric (i.e.  $\rho(A, B) = \rho(B, A)$ ).

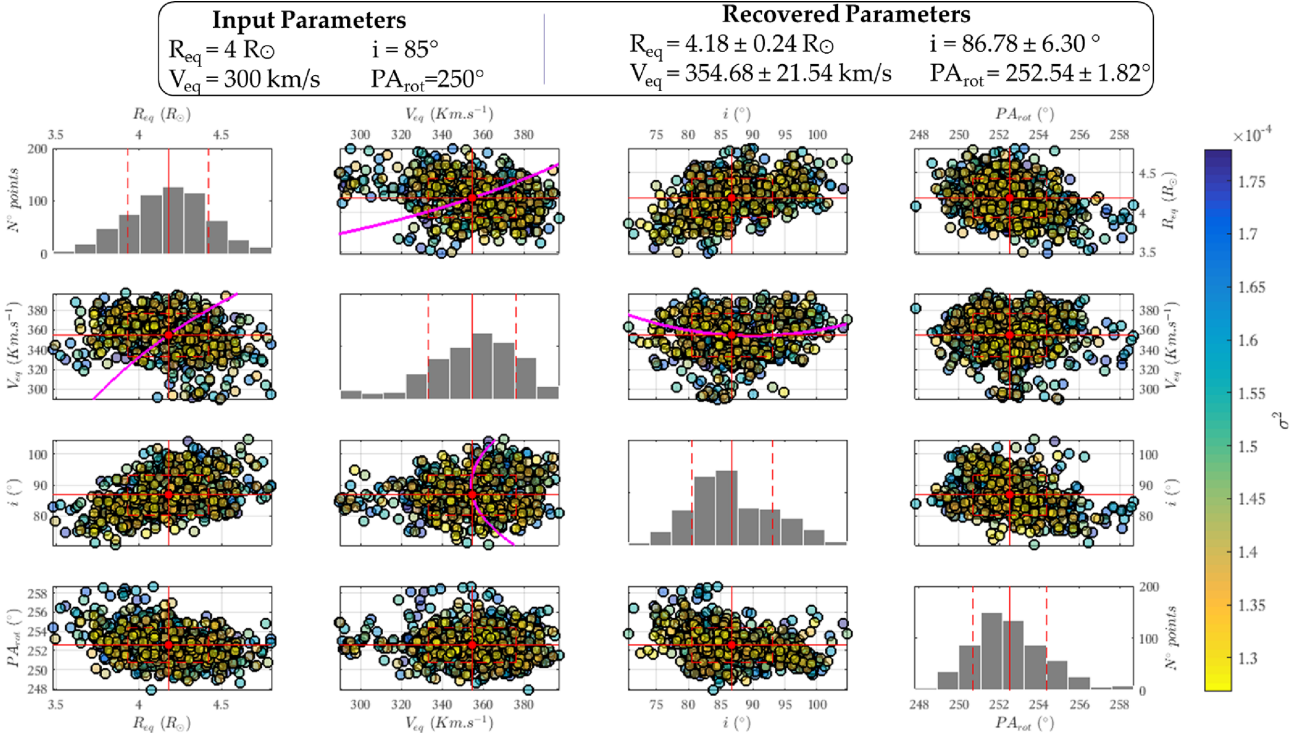


**Figure A1.** MCMC (DRAM) covariance matrix distribution results for the four free parameters ( $R_{\text{eq}}$ ,  $V_{\text{eq}}$ ,  $i$  and  $PA_{\text{rot}}$ ) of Regulus. The red point and line show the best recovered parameters, the average of the last MCMC run. The scatter plots show the projected two-dimensional distributions of the projected covariance matrix (coloured points) two by two parameters. The colour bar represents the distribution of the points around the average, following the variance  $\sigma^2$ . The histograms show the projected one-dimensional distributions, with solid red lines representing the best recovered parameters and dashed red line the uncertainties. From top to bottom and left to right, the panels show the equatorial radius  $R_{\text{eq}}$ , equatorial rotation velocity  $V_{\text{eq}}$ , rotation-axis inclination angle  $i$  and rotation-axis position angle  $PA_{\text{rot}}$ ; similarly, by symmetry, the histogram plots. The hypothetical behaviour of  $V_{\text{eq}} = f(i)$  is shown by a magenta continuous line following  $V_{\text{eq}} \sin i$ ; also  $R_{\text{eq}} = f(R_{\text{eq}})$ , which behaves theoretically as  $R_{\text{eq}} = R_{\text{p}} \left( 1 - V_{\text{eq}}^2 R_{\text{pol}} / 2GM \right)$ , is a magenta line. We observe that the distribution of the points is around those behaviours in both cases.

**APPENDIX B: SCIROCCO'S DEDUCED PARAMETERS**

Table B1 summarizes all the equations of the deduced parameters used by SCIROCCO, where  $G$  is the gravitational constant,  $\sigma$  the Stefan-Boltzmann constant and  $\theta$  the co-latitude (note that, for the critical equatorial rotation velocity, the Eddington factor can be ignored for Regulus, because it presents low luminosity).

**Table B1.** SCIROCCO's deduced parameter formulae.

Parameter	Formula
Angular diameter	$\mathcal{D}_{\text{eq}} = 2 \frac{R_{\text{eq}}}{d} \frac{180}{\pi} 36 \times 10^5 \text{ (3)}$
Equ-to-pol. radii	$\frac{R_{\text{pol}}}{R_{\text{eq}}} = \left(1 + \frac{V_{\text{eq}}^2 R_{\text{eq}}}{2GM}\right)^{-1} \text{ (1,2,3)}$
Critical radius	$R_{\text{crit}} = 3 \frac{R_{\text{p}}}{2} \text{ (1,2,3)}$
Crit. equa. rot. velocity	$V_{\text{crit}} = \sqrt{\frac{GM}{R_{\text{crit}}}} \text{ (1,2,3)}$
Latitudinal $T_{\text{eff}}$	$T_{\text{eff}}(\theta) = \left(\frac{C}{\sigma}\right)^{0.25} g_{\text{eff}}^{\beta}(\theta) \text{ (1,2,3)}$ where
	the constant $C = \frac{\sigma \bar{T}_{\text{eff}}^4 S_{\star}}{\int g_{\text{eff}}^{\beta}(\theta) dS}$
	and $T_{\text{eq}} = T_{\text{eff}}(90^{\circ})$
	and $T_{\text{pol}} = T_{\text{eff}}(0^{\circ} (+ 180^{\circ}))$
Luminosity	$\log L/L_{\odot} = \log \left( \frac{S_{\star} \sigma \bar{T}_{\text{eff}}^4}{4\pi R_{\odot}^2 \sigma T_{\odot}^4} \right) \text{ (3)}$

*Note:*

- (1) Domiciano de Souza et al. (2002)
- (2) Hadjara et al. (2014)
- (3) Hadjara (2015)

**APPENDIX C: ALL THE FIT RESULTS**

Table C1 summarizes all the fit results that we found for different parameter sets and methods.

**Table C1.** Parameters with their uncertainties estimated from Levenberg–Marquardt and MCMC fits for all the parameter sets.

Parameters		Comparison of best-fitting values between the four parameter sets				
Regulus		param_set 1	param_set 2	param_set 3	param_set 4	MCMC
<b>Best-fitting parameter</b>						
Equatorial radius $R_{\text{eq}}$		$4.16 \pm 0.08 R_{\odot}$	$4.00 \pm 0.18 R_{\odot}$	$4.16 \pm 0.11 R_{\odot}$	$4.00 \pm 0.17 R_{\odot}$	$4.18 \pm 0.24 R_{\odot}$
Equatorial rotation velocity $V_{\text{eq}}$		$317^{+3}_{-85} \text{ km s}^{-1}$	$358 \pm 16 \text{ km s}^{-1}$	$350 \pm 18 \text{ km s}^{-1}$	$358 \pm 13 \text{ km s}^{-1}$	$355 \pm 22 \text{ km s}^{-1}$
Rotation-axis inclination angle $i$		$90^{+0}_{-15} \circ$	$86.2 \pm 2.3^{\circ}$	$86.4 \pm 2.1^{\circ}$	$86.2 \pm 1.6^{\circ}$	$86.8 \pm 6.3^{\circ}$
Rotation-axis position angle		$265.5 \pm 2.8^{\circ}$	$251^{\circ}$	$251 \pm 10^{\circ}$	$251 \pm 5^{\circ}$	$253 \pm 2^{\circ}$
$P_{\text{hot}}$						
No. of free parameters		5 <sup>1</sup>	3	4	4	4
$\chi^2$		3.35 <sup>1</sup>	2.70	2.71	2.71	–
<b>Fixed parameter</b>						
Distance $d$		$23.5 \pm 0.4 \text{ pc}$	Value	23.759 $\pm$ 0.446 pc <sup>3</sup>		
Mass $M$		$3.39 \pm 0.24 M_{\odot}$		$3.8 \pm 0.57 M_{\odot}$		
Surface mean effective temperature $\bar{T}_{\text{eff}}$		12 250 K		12 500 K <sup>4</sup>		
Gravity-darkening coefficient $\beta$ Free						
<b>Limb-darkening parameters</b>						
Turbulent velocity $V_T$		–	Estimated	Estimated	0.25	Estimated
$\log g$		$\log g_{\text{eff}}=3.5 \text{ cm s}^{-2}$		$4 \text{ cm s}^{-2}$		
Claret $T_{\text{eff}}$		–		$2 \text{ km s}^{-1}$		
Metallicity $[\text{Fe}/\text{H}]^e$		–		10 500–15 000 K		
Spectral filter		–		0.0		
<b>Line profile</b>						
Kind		–		K		
Physical characteristics $[T_{\text{eff}}, \log g]$						
<b>Derived parameter</b>						
Equatorial angular diameter $\varpi_{\text{eq}}$		$1.65 \pm 0.02 \text{ mas}$	Estimated	Estimated	0.25	Estimated
Equatorial-to-polar radii		$1.32 \pm 0.04$		$4 \text{ cm s}^{-2}$		
$R_{\text{eq}}/R_{\text{pol}}$		$1.61^{+0.03}_{-0.02} \text{ mas}$		10 500 K, 4 cm s <sup>-2</sup>		
Critical radius $R_{\text{crit}}$		$1.31^{+0.05}_{-0.04}$		Value		
Critical equatorial rotation velocity $V_{\text{crit}}$		$4.72 \pm 0.04 R_{\odot}$		1.63 $\pm$ 0.04 mas		
$V_{\text{eq}} \sin i$		$369^{+14}_{-67} \text{ km s}^{-1}$		1.35 $\pm$ 0.06		
$V_{\text{eq}}/V_{\text{crit}}$		$317 \pm 3 \text{ km s}^{-1}$		1.35 $\pm$ 0.03		
$\beta$		$0.86 \pm 0.03$		1.35 $\pm$ 0.03		
Polar effective temperature $T_{\text{pol}}$		$0.25 \pm 0.11$		1.35 $\pm$ 0.06		
Equatorial effective temperature $T_{\text{eq}}$		$15 400 \pm 1400 \text{ K}$		1.35 $\pm$ 0.06		
Luminosity $\log(L/L_{\odot})$		$10 314 \pm 1000 \text{ K}$		1.35 $\pm$ 0.06		
		$2.540 \pm 0.043$		1.35 $\pm$ 0.06		
		$2.533^{+0.033}_{-0.037}$		1.35 $\pm$ 0.06		
		$2.463 \pm 0.034$		1.35 $\pm$ 0.06		
		$2.428 \pm 0.055$		1.35 $\pm$ 0.06		
		$2.461 \pm 0.031$		1.35 $\pm$ 0.06		
		$2.428 \pm 0.053$		1.35 $\pm$ 0.06		
		$2.464 \pm 0.069$		1.35 $\pm$ 0.06		

 Notes: <sup>1</sup> McAlister et al. (2005);

<sup>2</sup> Che et al. (2011);

<sup>3</sup> Perryman et al. (1997);

<sup>4</sup> Malagnini & Morossi (1990);

<sup>5</sup> theoretical estimate of  $\beta$  from Espinosa Lara & Rieutord (2011).

 This paper has been typeset from a  $\text{\LaTeX}$  file prepared by the author.